

1 Non-Hydrostatic RegCM4 (RegCM4-NH): Model description and  
2 case studies over multiple domains.

3 Coppola E. (1), Stocchi P. (2), Pichelli E. (1), Torres A. (1), Glazer R. (1), Giuliani G. (1),  
4 F. Di Sante (1), R. Nogherotto (1), Giorgi F. (1)

5

6 *Correspondence to:* Erika Coppola ([coppolae@ictp.it](mailto:coppolae@ictp.it))

7 1. International Centre for Theoretical Physics (ICTP), Trieste, Italy

8 2. Institute of Atmospheric Sciences and Climate, National Research Council of Italy,  
9 CNR-ISAC, Bologna, Italy

10 **Abstract.** We describe the development of a non-hydrostatic version of the regional  
11 climate model RegCM4, called RegCM4-NH, for use at convection-permitting resolutions.  
12 The non-hydrostatic dynamical core of the Mesoscale Model MM5 is introduced in the  
13 RegCM4, with some modifications to increase stability and applicability of the model to  
14 long-term climate simulations. Newly available explicit microphysics schemes are also  
15 described, and three case studies of intense convection events are carried out in order to  
16 illustrate the performance of the model. They are all run at convection-permitting grid  
17 spacing of 3 km over domains in northern California, Texas and the Lake Victoria region,  
18 without the use of parameterized cumulus convection. A substantial improvement is found  
19 in several aspects of the simulations compared to corresponding coarser resolution (12  
20 km) runs completed with the hydrostatic version of the model employing parameterized  
21 convection. RegCM4-NH is currently being used in different projects for regional climate  
22 simulations at convection-permitting resolutions, and is intended to be a resource for  
23 users of the RegCM modeling system.

24

25 **Keywords**

26 Regional climate models; RegCM4; km-scale resolution; climate change

## 27 **Introduction**

28 Since the pioneering work of Dickinson et al. (1989) and Giorgi and Bates (1989),  
29 documenting the first regional climate modeling system (RegCM, version 1) in literature,  
30 the dynamical downscaling technique based on limited area Regional Climate Models  
31 (RCMs) has been widely used worldwide, and a number of RCM systems have been  
32 developed (Giorgi 2019). RegCM1 (Dickinson et al., 1989, Giorgi and Bates, 1989) was  
33 originally developed at the National Center for Atmospheric Research (NCAR) based on  
34 the Mesoscale Model version 4 (MM4) (Anthes et al, 1987) . Then, further model versions  
35 followed: RegCM2 (Giorgi et al. 1993a,b), RegCM2.5, (Giorgi and Mearns 1999),  
36 RegCM3 (Pal et al. 2007), and lastly RegCM4 (Giorgi et al 2012). Except for the transition  
37 from RegCM1 to RegCM2, in which the model dynamical core was updated from that of  
38 the MM4 to that of the MM5 (Grell et al. 1995), these model evolutions were mostly based  
39 on additions of new and more advanced physics packages. RegCM4 is today used by a  
40 large community for numerous projects and applications, from process studies to paleo  
41 and future climate projections, including participation in the Coordinated Regional  
42 Downscaling EXperiment (CORDEX, Giorgi et al. 2009; Gutowski et al. 2016). The model  
43 can also be coupled with ocean, land and chemistry/aerosol modules in a fully interactive  
44 way (Sitz et al. 2017).

45 The dynamical core of the standard version of RegCM4 is hydrostatic, with sigma-p  
46 vertical coordinates. As a result, the model can be effectively run for grid spacings of ~10  
47 km or larger, for which the hydrostatic assumption is valid. However, the RCM community  
48 is rapidly moving to higher resolutions of a few km, i.e. “convection-permitting” (Prein et  
49 al. 2015; Coppola et al. 2020) and therefore the dynamical core of RegCM4 has been  
50 upgraded to include a non-hydrostatic dynamics representation usable for very high  
51 resolution applications. This upgrade, which we name RegCM4-NH, is essentially based  
52 on the implementation of the MM5 non-hydrostatic dynamical core within the RegCM4  
53 framework, which has an entirely different set of sub-grid model physics compared to  
54 MM5.

55

56 RegCM4-NH is already being used in some international projects focusing on climate  
57 simulations at convection-permitting km-scales, namely the European Climate Prediction

58 System (EUCP, Hewitt and Lowe 2018) and the CORDEX Flagship Pilot Study dedicated  
59 to convection (CORDEX-FPSCONV, Coppola et al. 2020), and it is starting to be used  
60 more broadly by the RegCM modeling community.

61 For example, the recent papers by Ban et al. (2021) and Pichelli et al. (2021) document  
62 results of the first multi-model experiment of 10-year simulations at the convection-  
63 permitting scales over the so-called greater Alpine region. Two different simulations with  
64 RegCM4-NH for present day conditions have contributed to the evaluation analysis of  
65 Ban et al. (2021). They were carried out at the International Centre for Theoretical Physics  
66 (ICTP) and the Croatian Meteorological and Hydrological Service (DHMZ) using two  
67 different physics configurations. The results show that RegCM4-NH largely improves the  
68 precipitation simulation as compared to available fine scale observations when going from  
69 coarse to high resolution, in particular for higher order statistics, such as precipitation  
70 extremes and hourly intensity. Pichelli et al. (2021) then analyse multi-model ensemble  
71 simulations driven by selected CMIP5 GCM projections for the decades 1996–2005 and  
72 2090–2099 under the RCP8.5 scenario. ICTP contributed to the experiment with  
73 simulations using RegCM4-NH driven by the MOCH-HadGEM GCM (r1i1p1) in a two  
74 level nest configuration (respectively at 12 and 3 km grid). The paper shows new insights  
75 into future changes, for example an enhancement of summer and autumn hourly rainfall  
76 intensification compared to coarser resolution model experiments, as well as an increase  
77 of frequency and intensity of high-impact weather events.

78  
79 In this paper we describe the structure of RegCM4-NH and provide some illustrative  
80 examples of its performance, so that model users can have a basic reference providing  
81 them with background information on the model. In the next section we first describe the  
82 new model dynamical core, while the illustrative applications are presented in section 4.  
83 Section 5 finally provides some discussion of future developments planned for the RegCM  
84 system.

85

## 86 **Model description**

87 In the development of RegCM4-NH, the RegCM4 as described by Giorgi et al. (2012) was  
88 modified to include, the non-hydrostatic dynamical core (*idynamic* = 2 namelist option as  
89 described in RegCM-4.7.1/Doc/README.namelist of the source code) of the mesoscale  
90 model MM5 (Grell et al. 1995). This dynamical core was selected because RegCM4  
91 already has the same grid and variable structure as MM5 in its hydrostatic core, which  
92 substantially facilitated its implementation (Elguindi et al. 2017).

93

94 The model equations with complete description of the Coriolis force and a top radiative  
95 boundary condition, along with the finite differencing scheme, are given in Grell et al.  
96 (1995). Pressure,  $p$ , temperature,  $T$ , and density,  $\rho$ , are first decomposed into a  
97 prescribed reference vertical profile plus a time varying perturbation. The prognostic  
98 equations are then calculated using the pressure perturbation values. Compared to the  
99 original MM5 dynamical core, the following modifications were implemented in order to  
100 achieve increased stability for long term climate simulations (Elguindi et al. 2017  
101 document any modifications which follow the choice of the non-hydrostatic dynamical  
102 core through the namelist parameter *idynamic* = 2; further available user-dependant  
103 options, and the corresponding section in the namelist, are explicitly indicated):

104

105 i) The reference state temperature profile is computed using a latitude dependent  
106 climatological temperature distribution and thus is a function of the specific domain  
107 coordinates (*base\_state\_pressure*, *logp\_lrate* parameters in *&referenceatm*) (Elguindi et  
108 al. 2017). These two parameters were hard-coded in the original MM5 while for the  
109 RegCM are user configurable;

110

111 ii) The lateral time dependent boundary conditions (*iboudy* in *&physicsparam*) for each  
112 prognostic variable use the same exponential relaxation technique (*iboudy* = 5) described  
113 in Giorgi et al. (1993). The linear MM5 relaxation scheme is also kept as an option (*iboudy*  
114 = 1);

115

116 iii) The advection term in the model equations, which in the MM5 code is implemented  
 117 using a centered finite difference approach, was changed to include a greater upstream  
 118 weight factor as a function of the local Courant number (Elguindi et al. 2017). The  
 119 maximum value of the weight factor is user configurable (*uoffc* in *&dynparam*). As detailed  
 120 in the MM5 model description (Grell et al, 1995), the horizontal advection term for a scalar  
 121 variable  $X$  contributes to the total tendency as:

$$\Delta_{adv}(p^*X)_G = -m^2|_G \left[ \frac{(p^*X|_{b\frac{u}{m}}|_b - p^*X|_{a\frac{u}{m}}|_a)}{dx} + \frac{(p^*X|_{d\frac{v}{m}}|_d - p^*X|_{c\frac{v}{m}}|_c)}{dy} \right]$$

122  
 123  
 124  
 125 where the  $m$  is the projection mapping factor and, with respect to Figure 1, assuming that  
 126 the computation is to be performed for the gold cross point  $G$ , the averages are performed  
 127 in the points  $a, b, c, d$ . For the  $u/m$  and  $v/m$  terms, the average value is computed using  
 128 respectively the values in points  $AC, BD, CD, AB$ .

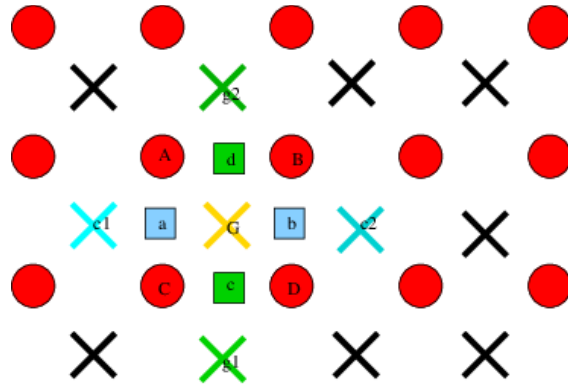
129 In RegCM4 for the term  $p^*X$ , the model computes a weighted average value of the field  
 130 using the value in gold+cyan and gold+green cross points with weights increasing the  
 131 relative contribution of the upstream point up as a function of the local courant number:

$$\begin{aligned} 132 & \\ 133 & p^*X|_a = 0.5((1 - f_1)p^*X|_G + (1 + f_1)p^*X|_{c_1}) \\ 134 & p^*X|_b = 0.5((1 - f_1)p^*X|_{c_2} + (1 + f_1)p^*X|_G) \\ 135 & p^*X|_c = 0.5((1 - f_2)p^*X|_G + (1 + f_2)p^*X|_{g_1}) \\ 136 & p^*X|_d = 0.5((1 - f_2)p^*X|_{g_2} + (1 + f_2)p^*X|_G) \end{aligned}$$

137 where  $f_1, f_2$  are defined as the local Courant number for the 1D advection equations  
 138 multiplied for a control factor:

$$\begin{aligned} 139 & \\ 140 & f_1 = \mu_{fc}dt \frac{(u|_a + u|_b)}{2dx} \\ 141 & f_2 = \mu_{fc}dt \frac{(v|_c + v|_d)}{2dy} ; \end{aligned}$$

142  
 143



144

145 **Figure 1 Schematic representation showing the horizontal advection scheme**  
 146 **staggering. Circles are U,V points. X are scalar variable points.**

147

148

149 iv) The moisture term uses the same advection scheme as the other variables (Elguindi  
 150 et al. 2017) and not a complete upstream scheme as in the MM5 code (Grell et al. 1995);

151

152 v) A local flux limiter reduces the advection terms in order to remove unrealistic strong  
 153 gradients and its limits are user configurable (in the *&dynparam* section the maximum  
 154 gradient fraction for advection: temperature, *t\_extrema*, specific humidity, *q\_rel\_extrema*,  
 155 liquid cloud content, *c\_rel\_extrema* and for tracers, *t\_rel\_extrema*). This was hardcoded  
 156 in the MM5 code and the limits were not user configurable;

157

158 vi) The diffusion stencil of the Laplace equation uses a nine point approach as in LeVeque  
 159 (2006) and a topography dependent environmental diffusion coefficient is added to  
 160 reduce spurious diffusion along pressure coordinate slopes (Elguindi et al. 2017) as in  
 161 the hydrostatic version of the code (Giorgi et al. 1993b). The change in stencil does not  
 162 affect the overall fourth order precision of the model, but reduces the computational  
 163 stencil size, thus reducing the communication overhead;

164

165 vii) The top boundary radiative condition (*ifupr = 1* in *&nonhydroparam*) adopted in the  
 166 semi-implicit vertical differencing scheme to reduce the reflection of energy waves uses  
 167 coefficients on a 13x13 matrix which are re-computed every simulation day and not kept  
 168 constant throughout the whole simulation as in the MM5 code. This allows the model to

169 be run for longer simulation times while not being strongly tied to the initial atmospheric  
 170 conditions;

171  
 172 viii) The dynamical control parameter  $\beta$  in the semi-implicit vertical differencing scheme  
 173 (*nhbet* in *&nonhydroparam*) used for acoustic wave damping (Elguindi et al. 2017) is user  
 174 configurable (Klemp and Dudhia, 2008), while it is hard-coded in the MM5;

175  
 176 ix) A Rayleigh damping (*ifrayd* = 1 in *&nonhydroparam*) of the status variables towards  
 177 the input GCM boundary conditions can be activated in the top layers (*rayndamp*  
 178 configuring the number of top levels to apply) with a configurable relaxation time  
 179 (*rayalpha0*, Klemp and Lilly, 1978, Durran and Klemp, 1983. This is consistent to what is  
 180 implemented in the WRF model);

181  
 182 x) The water species time filtering uses the Williams (2009) modified filter with  $\alpha = 0.53$   
 183 instead of the RA filter used by all the other variables. The  $v$  factor in the RA filter is user  
 184 configurable (*gnu1* and *gnu2* in *&dynparam*). This reduces the damping introduced by the  
 185 Robert-Asselin filter and the computational diffusion introduced by the horizontal  
 186 advection scheme.

187  
 188 With these modifications, the model basic equations, under leap-frog integration scheme,  
 189 are (Elguindi et al. 2017) :

190  
 191

$$\frac{\partial p^* u}{\partial t} = -m^2 \left[ \frac{\partial p^* u u / m}{\partial x} + \frac{\partial p^* v u / m}{\partial y} \right] - \frac{\partial p^* u \dot{\sigma}}{\partial \sigma} + u \text{DIV} - \frac{m p^*}{\rho} \left[ \frac{\partial p'}{\partial x} - \frac{\sigma}{p^*} \frac{\partial p^*}{\partial x} \frac{\partial p'}{\partial \sigma} \right] + p^* f v - p^* e w \cos \theta + D_u \quad (1)$$

192  
 193

$$\frac{\partial p^* v}{\partial t} = -m^2 \left[ \frac{\partial p^* u v / m}{\partial x} + \frac{\partial p^* v v / m}{\partial y} \right] - \frac{\partial p^* v \dot{\sigma}}{\partial \sigma} + v \text{DIV} - \frac{m p^*}{\rho} \left[ \frac{\partial p'}{\partial y} - \frac{\sigma}{p^*} \frac{\partial p^*}{\partial y} \frac{\partial p'}{\partial \sigma} \right] - p^* f u + p^* e w \sin \theta + D_v \quad (2)$$

194

195

$$\frac{\partial p^* w}{\partial t} = -m^2 \left[ \frac{\partial p^* u w / m}{\partial x} + \frac{\partial p^* v w / m}{\partial y} \right] - \frac{\partial p^* w \dot{\sigma}}{\partial \sigma} + w DIV +$$

$$p^* g \frac{\rho_0}{\rho} \left[ \frac{1}{p^*} \frac{\partial p'}{\partial \sigma} + \frac{T'_v}{T} - \frac{T_0 p'}{T p_0} \right] - p^* g [(q_c + q_r)] + p^* e (u \cos \theta - v \sin \theta) + D_w \quad (3)$$

196

197

$$\frac{\partial p^* p'}{\partial t} = -m^2 \left[ \frac{\partial p^* u p' / m}{\partial x} + \frac{\partial p^* v p' / m}{\partial y} \right] - \frac{\partial p^* p' \dot{\sigma}}{\partial \sigma} + p' DIV -$$

$$m^2 p^* \gamma p \left[ \frac{\partial u / m}{\partial x} - \frac{\sigma}{m p^*} \frac{\partial p^*}{\partial x} \frac{\partial u}{\partial \sigma} + \frac{\partial v / m}{\partial y} - \frac{\sigma}{m p^*} \frac{\partial p^*}{\partial y} \frac{\partial v}{\partial \sigma} \right] + \rho_0 g \gamma p \frac{\partial w}{\partial \sigma} + p^* \rho_0 g \quad (4)$$

198

199

$$\frac{\partial p^* T}{\partial t} = -m^2 \left[ \frac{\partial p^* u T / m}{\partial x} + \frac{\partial p^* v T / m}{\partial y} \right] - \frac{\partial p^* T \dot{\sigma}}{\partial \sigma} + T DIV +$$

$$\frac{1}{\rho c_p} \left[ p^* \frac{D p'}{D t} - \rho_0 g p^* w - D_{p'} \right] + p^* \frac{\dot{Q}}{c_p} + D_T \quad (5)$$

200

201

202 Where:

$$DIV = m^2 \left[ \frac{\partial p^* u / m}{\partial x} + \frac{\partial p^* v / m}{\partial y} \right] + \frac{\partial p^* \dot{\sigma}}{\partial \sigma}$$

203

$$\dot{\sigma} = -\frac{\rho_0 g}{p^*} w - \frac{m \sigma}{p^*} \frac{\partial p^*}{\partial x} u - \frac{m \sigma}{p^*} \frac{\partial p^*}{\partial y} v$$

204

$$\tan \theta = -\cos \phi \frac{\partial \lambda / \partial y}{\partial \phi / \partial x}$$

205

$$p(x, y, z, t) = p_0(z) + p'(x, y, z, t)$$

$$T(x, y, z, t) = T_0(z) + T'(x, y, z, t)$$

$$\rho(x, y, z, t) = \rho_0(z) + \rho'(x, y, z, t)$$

206

207

208 with the vertical sigma coordinate defined as:

209

$$\sigma = \frac{(p_0 - p_t)}{(p_s - p_t)}$$

210

211

212  $p_s$  is the surface pressure and  $p_0$  is the reference pressure profile. The total pressure

213 at each grid point is thus given as:



214

215 
$$p(x, y, z, t) = p^* \sigma(k) + p_t + p'(x, y, z, t)$$

216

217 With  $p_t$  being the top model pressure assuming a fixed rigid lid.

218 The model physics schemes for boundary layer, radiative transfer, land and ocean  
219 surface processes, cloud and precipitation processes are extensively described in Giorgi  
220 et al. (2012) and summarized in Table 1. For each physics component a number of  
221 parameterization options are available (Table 1), and can be selected using a switch  
222 selected by the user. As mentioned, the use of non-hydrostatic dynamics is especially  
223 important when going to convection-permitting resolutions of a few km (Prein et al. 2015).  
224 At these resolutions the scale separation assumption underlying the use of cumulus  
225 convection schemes is not valid any more, and explicit cloud microphysics  
226 representations are necessary. The RegCM4 currently includes two newly implemented  
227 microphysics schemes, the Nogherotto-Tompkins (Nogherotto et al. 2016) and the WSM5  
228 scheme from the Weather Research Forecast (WRF, Skamarok et al. 2008) model, which  
229 are briefly described in the next sections for information to model users.

230

<b>Model physics</b> ( <i>Namelist flag</i> )	<b>Options</b>	<i>n. option</i>	<b>Reference</b>
<b>Dynamical core</b> ( <i>idynamic</i> )	Hydrostatic	1	Giorgi et al. 1993a,b Giorgi et al. 2012
	Non-Hydrostatic (*)	2	present paper
<b>Radiation</b> ( <i>irrtm</i> )	CCSM	0	Kiehl et al. 1996
	RRTM (*)	1	Mlawer et al. 1997
<b>Microphysics</b>	Subex	1	Pal et al 2000

<i>(ipptls)</i>	Nogherotto Thompkins	2	Nogherotto et al. 2016
	WSM5 (*)	3	Hong et al 2004
<b>Cumulus</b> <i>(icup)</i>	Kuo	1	Anthes et al. 1987
	Grell	2	Grell 1993
	Emanuel	4	Emanuel 1991
	Tiedtke	5	Tiedtke 1989, 1993
	Kain-Fritsch	6	Kain and Fritsch, 1990; Kain 2004
	MM5 Shallow cumulus (only mixing) (*)	-1	Grell et al. 1994
<b>Planetary Boundary Layer</b> <i>(ibltyp)</i>	Modified-Holtslag	1	Holtslag et al., 1990
	UW	2	Bretherton et al. 2004
<b>Land Surface</b> <i>(code compiling option)</i>	BATS	/	Dickinson et al. 1993; Giorgi et al. 2003
	CLM4.5	/	Oleson et al. 2013
<b>Ocean Fluxes</b> <i>(iocnflx)</i>	BATS	1	Dickinson et al. 1993
	Zeng	2	Zeng et al. 1998
	COARE	3	Fairall et al. 1996a,b

<b>Interactive lake</b> ( <i>lakemod</i> )	1D diffusion/convection	1	Hostetler et al. 1993
<b>Tropical band</b> ( <i>i_band</i> )	RegT-Band	1	Coppola et al. 2012
<b>Coupled ocean</b> ( <i>iocncpl</i> )	RegCM-ES	1	Sitz et al. 2017

231 **Table 1 Core and sub-grid physics scheme available in RegCM-NH. New schemes**  
232 **available with this release are starred (\*).**

233

234

235 **Explicit microphysics schemes**

236 ***Nogherotto-Tompkins Scheme***

237 A new parameterization for explicit cloud microphysics and precipitation built upon the  
238 European Centre for Medium Weather Forecast's Integrated Forecast System (IFS)  
239 module (Tiedtke [1993], Tompkins [2007]), was introduced in RegCM4 (*ipptls* = 2 in  
240 *&microparam*) by Nogherotto et al. [2016]. In the present configuration, the scheme  
241 implicitly solves 5 prognostic equations for water vapor, *qv*, cloud liquid water, *ql*, rain, *qr*,  
242 cloud ice, *qi*, and snow, *qs*, but it is also easily extendable to a larger number of variables.  
243 Water vapor, cloud liquid water, rain, cloud ice and snow are all expressed in terms of the  
244 grid-mean mixing ratio.

245 Cloud liquid and ice water content are independent, allowing the existence of supercooled  
246 liquid water and mixed-phase clouds. Rain and snow precipitate with a fixed terminal fall  
247 speed and can then be advected by the three dimensional winds. A check for the  
248 conservation of enthalpy and of total moisture is ensured at the end of each timestep. The  
249 governing equation for each variable is:

250

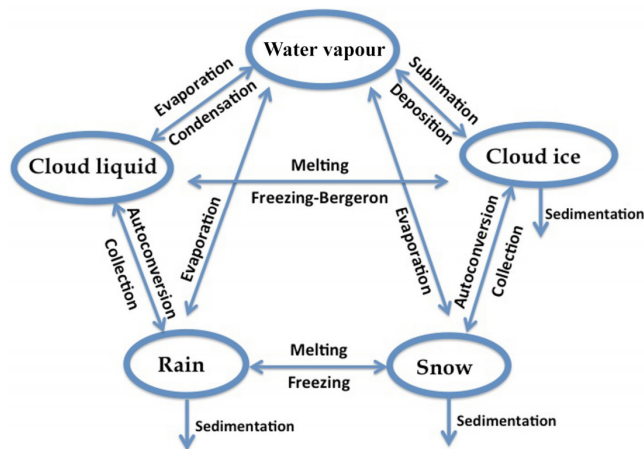
$$\frac{\partial q_x}{\partial t} = S_x + \frac{1}{\rho} \frac{\partial}{\partial z} (\rho V_x q_x)$$

251

252

253 The local variation of the mixing ratio  $q_x$  of the variable  $x$  is given by the sum of  
 254  $S_x$ , containing the net sources and sinks of  $q_x$  through microphysical processes (i.e.  
 255 condensation, evaporation, auto-conversion, melting, etc.), and the sedimentation term,  
 256 which is a function of the fall speed  $V_x$ . An upstream approach is employed to solve the  
 257 equations. The sources and sinks contributors are divided in two groups according to the  
 258 duration of the process they describe: processes that are considered to be fast relative to  
 259 the model time step are treated implicitly while slow processes are treated explicitly. The  
 260 processes taken into account (shown in Figure 2) are the microphysical pathways across  
 261 the 5 water variables: condensation, autoconversion, evaporation, cloud water collection  
 262 (accretion), and autoconversion for warm clouds, and freezing, melting, deposition,  
 263 sublimation for cold clouds.

264



265

266 **Figure 2: Depiction of the new scheme, showing the five prognostic variables and**  
 267 **how they are related to each other through microphysical processes**

268 For each microphysical pathway, phase changes are associated with the release or  
 269 absorption of latent heat, which then impacts the temperature budget. The impact is

270 calculated using the conservation of liquid water temperature TL defined as:  
271

$$272 \quad T_L = T - \frac{L_v}{C_p}(q_l + q_r) - \frac{L_s}{C_p}(q_i + q_s).$$

273 Given that  $dTL = 0$ , the rate of change of the temperature is given by the following  
274 equation:

275

$$276 \quad \frac{\partial T}{\partial t} = \sum_{x=1}^m \frac{L(x)}{C_p} \left( \frac{dq_x}{dt} - D_{q_x} - \frac{1}{\rho} \frac{\partial}{\partial z} (\rho V_x q_x) \right)$$

277

278 where  $L(x)$  is the latent heat of fusion or evaporation, depending on the process  
279 considered,  $D_{q_x}$  is the convective detrainment and the third term in brackets is the  
280 sedimentation term.

281 At the end of each time step a check is carried out of the conservation of total water and  
282 moist static energy:  $h = C_p T + gz + Lq_x$ .

283 The scheme is tunable through parameters in the *&microparam* section of the namelist  
284 (RegCM-4.7.1/Doc/README.namelist; Elguindi et al. 2017).

285

## 286 **WSM5 Scheme**

287 RegCM4-NH also employs the Single-Moment 5-class microphysics scheme of the WRF  
288 model (Skamarock et al., 2008). This scheme (*ipptls* = 3 in *&microparam*) follows Hong  
289 et al. (2004) and, similarly to Nogherotto et al. (2016), includes vapor, rain, snow, cloud  
290 ice, and cloud water hydrometeors. The scheme separately treats ice and water  
291 saturation processes, assuming water hydrometeors for temperatures above freezing,  
292 and cloud ice and snow below the freezing level (Dudhia, 1989, Hong et al., 1998). It  
293 accounts for supercooled water and a gradual melting of snow below the melting layer

294 (Hong et al., 2004, and Hong and Lim, 2006). Therefore, the WSM5 and Nogherotto-  
295 Tompkins schemes have similar structures (Figure 1), but also important differences.

296 Differently from the Nogherotto-Tompkins scheme, the WSM5 (as well as the other WSM  
297 schemes in WRF) prescribes an inverse exponential continuous distribution of particle  
298 size (ex. Marshall and Palmer (1948) for rain, Gunn and Marshall (1958) for snow). It also  
299 includes the size distribution of ice particles and, as a major novelty, the definition of the  
300 number of ice crystals based on ice mass content rather than temperature. Both the  
301 Nogherotto-Tompkins and WSM5 schemes include autoconversion, i.e. sub-time step  
302 processes of conversion of cloud water to rain and cloud ice to snow. For rain, Hong et  
303 al. (2004) use a Kessler (1969) type algorithm in WSM5, but with a stronger physical basis  
304 following Tripoli and Cotton (1980). The Nogherotto-Tompkins scheme also includes the  
305 original Kessler (1969) formula as an option, but it makes available other three  
306 exponential approaches following Sundqvist et al. (1989), Beheng (1994), and  
307 Khairoutdinov and Kogan (2000). For ice autoconversion the Nogherotto-Tompkins  
308 scheme uses an exponential approach (Sundqvist, 1989) with a specific coefficient for ice  
309 particles (following Lin et al., 1983) depending on temperature, while the WSM5 uses a  
310 critical value of ice mixing ratio (depending on air density) and a maximum allowed ice  
311 crystal mass (following Rutledge and Hobbs, 1983) that suppresses the process at low  
312 temperatures because of the effect of air density. Finally, the WSM5 has no dependency  
313 on cloud cover for condensation processes while the Nogherotto-Tompkins scheme uses  
314 cloud cover to regulate the condensation rate in the formation of stratiform clouds.

315

### 316 ***Illustrative case studies***

317

318 Three case studies (Table 2) of Heavy Precipitation Events (HPE) have been identified in  
319 order to test and illustrate the behavior of the non-hydrostatic core of the RegCM4-NH,  
320 with focus on the explicit simulation of convection over different regions of the world. In  
321 two of the test cases, California and Lake Victoria, data from the ERA-Interim reanalysis  
322 (Dee et al. 2011) are used to provide initial and lateral meteorological boundary conditions

323 (every 6 hours) for an intermediate resolution run (grid spacing of 12 km, with use of  
324 convection parameterizations), which then provides driving boundary conditions for the  
325 convection-permitting experiments (Figure 3). In the Texas case study, however, we  
326 nested the model directly in the ERA-Interim reanalysis given that such configuration was  
327 able to accurately reproduce the HPE intensity. In this case the model uses a large LBC  
328 relaxation zone which allows the description of realistic fine-scale features driving this  
329 weather event (although not fully consistent with the Matte et al. (2017) criteria). All  
330 simulations start 24-48 hours before the HPE (Table 2). The analysis focuses on the total  
331 accumulated precipitation over the entire model domain at 3 km resolution (Figure 2) for  
332 the periods defined in Table 2. In the cases of California and Texas the evaluation also  
333 includes the time series of 6 hourly accumulated precipitation averaged on the region of  
334 maximum precipitation (black rectangles in Figures 5a and 7a) because high temporal  
335 resolution observations (NCEP/CPC) are also available (Table 3). The discussion of the  
336 case studies is presented in the next sections; the configuration files (namelists) with full  
337 settings for the three test cases are available at <https://zenodo.org/record/5106399>.

338

339 A key issue concerning the use of CP-RCMs is the availability of very high resolution,  
340 high quality observed datasets for the assessment and evaluation of the models, which  
341 is lacking for most of the world regions. Precipitation measurements come from  
342 essentially three distinct sources: in-situ rain-gauges, ground radar and satellite. In the  
343 present study we use 7 observational datasets depending on the case study and the area  
344 covered, as described in Table 3. We have used: Precipitation Estimation from Remotely  
345 Sensed Information using Artificial Neural Networks - Climate Data Record (PERSIAN-  
346 CDR), Climate Hazards Group InfraRed Precipitation with Station data (CHIRPS), the  
347 Climate Prediction Center morphing method (CMORPH), Tropical Rainfall Measuring  
348 Mission (TRMM), NCEP/CPC-Four Kilometer Precipitation Set Gauge and Radar  
349 (NCEP/CPC), CPC-Unified gauge-based daily precipitation estimates (CPC) and  
350 Parameter-elevation Regressions on Independent Slopes Model (PRISM) (Table 3).  
351 NCEP/CPC is a precipitation analysis which merges a rain gauge dataset with radar  
352 estimates. CMORPH and PERSIAN-CDR are based on satellite measurements, CHIRPS  
353 incorporates satellite imagery with in-situ station data. CPC is a gauge-based analysis of

354 daily precipitation. The PRISM dataset gathers climate observations from a wide range  
 355 of monitoring networks, applying sophisticated quality control measures and developing  
 356 spatial climate datasets which incorporate a variety of modeling techniques at multiple  
 357 spatial and temporal resolutions.

358

Case	ACRONYM	Region of The event	Domains size lon x lat x vertical levels	Simulation Time Window (UTC)
1	CAL	California	480 x 440 x 41	15 Feb 2004 00:00 19 Feb 2004 00:00
2	TEX	Texas	480 x 440 x 41	9 June 2010 00:00 12 June 2010 00:00
3	LKV	Lake Victoria	550 x 530 x 41	25 Nov 1999 00:00 1 Dec 1999 00:00

359 **Table 2: List of acronyms and description of the test cases with corresponding**  
 360 **3km domain sizes and simulation period.**

361

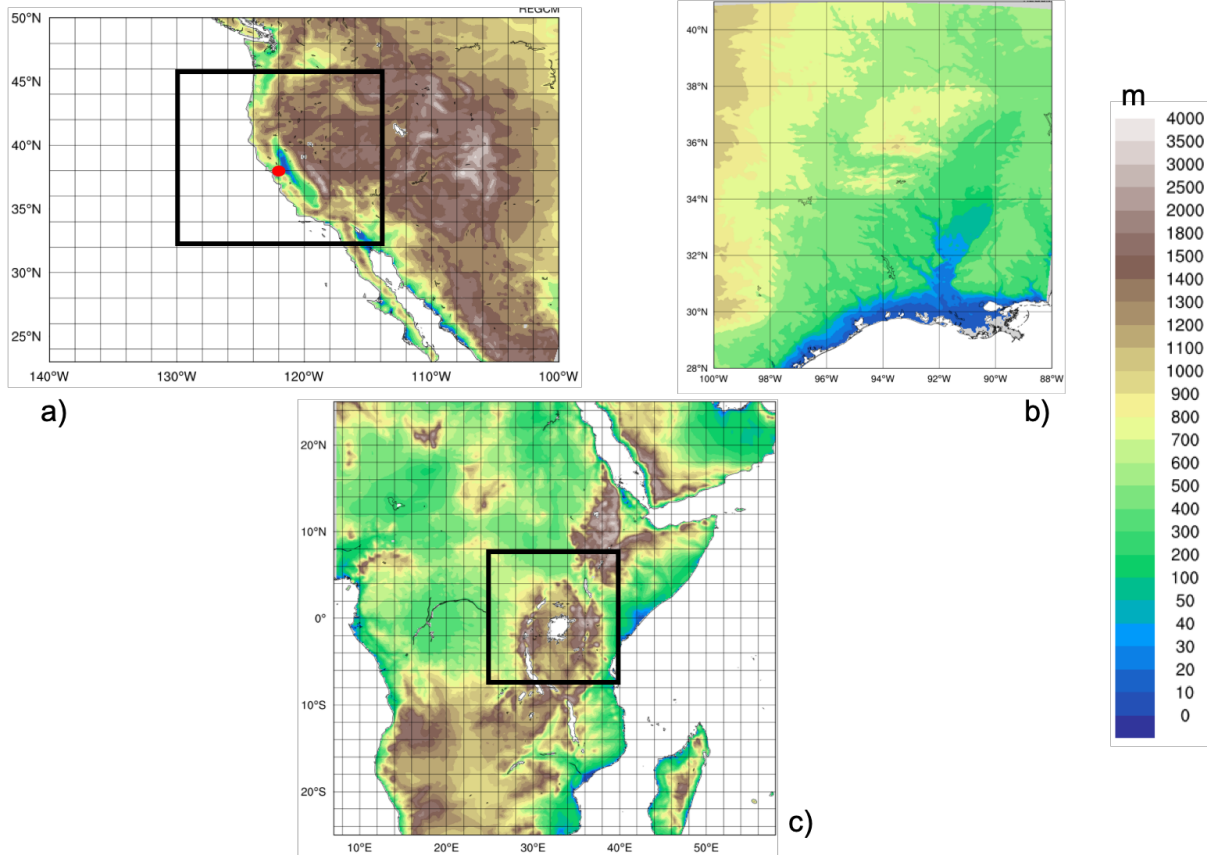
Dataset name	Region	Spatial Resolution	Temporal Resolution	Data Source	Reference
TRMM	World	0.5°	Daily	Satellite	Huffman et al. (2007)
CHIRPS	World	0.05°	Daily	Station data+Satellite	Funk et al. (2015)
CMORPH	World	0.25°	Daily	Satellite	Joyce et al.



					(2004)
NCEP/CPC	USA	0.04°	Hourly	<i>Gauge and Radar</i>	<a href="https://doi.org/10.5065/D69Z93M3">https://doi.org/10.5065/D69Z93M3</a> . Accessed: 27/06/2018
CPC	World	0.5°	Daily	Station data	Chen and Xie (2008)
PRISM	USA	0.04°	Daily	Station data	PRISM Climate Group. 2016.
PERSIAN-CDR	World	0.25°	Daily	Satellite	Ashouri et al. (2015)

362 **Table 3: List of observed precipitation datasets used for comparison.**

363



364

365 **Figure 3: Domains tested , a) California (CAL) , b) Texas (TEX), c) Lake Victoria**  
 366 **(LKV) . For CAL (a) and LKV (b) the black square shows the 3 km simulation**  
 367 **domains nested in the 12 km domain in figure. For TEX case (b) the 3 km**  
 368 **simulation (b) is fed directly with the ERA-Interim reanalysis fields.**

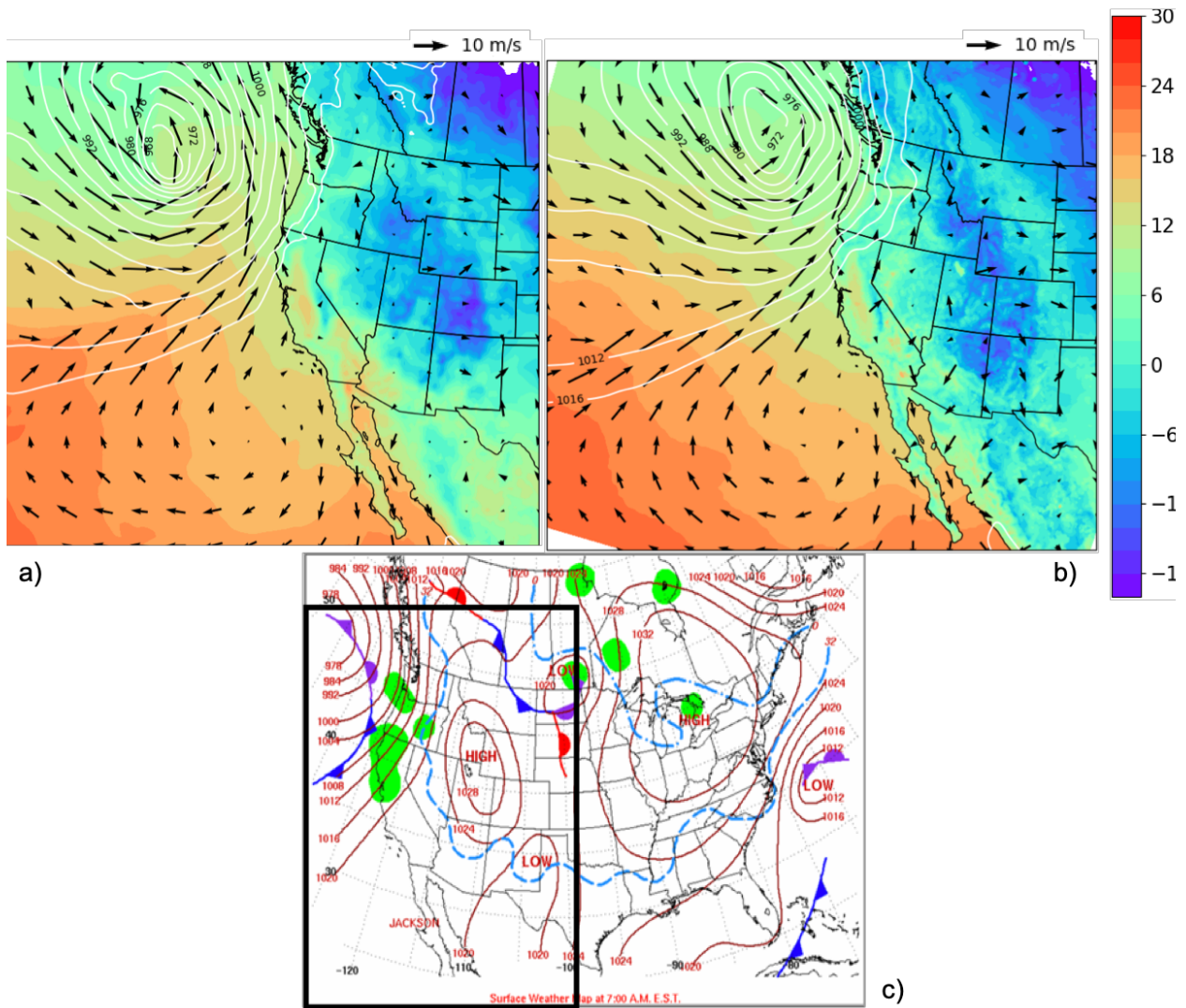
369

370

### 371 **California**

372 The first case, referred to as CAL in Table 2, is a HPE which occurred on February 16-18  
 373 2004, producing flooding conditions for the Russian River, a southward-flowing river in  
 374 the Sonoma and Mendocino counties of northern California (red-dot in Figure 3a). The  
 375 event is documented in detail by Ralph et al. (2006), who focused their attention on the  
 376 impact of narrow filament-shaped structures of strong horizontal water vapor transport  
 377 over the eastern Pacific Ocean and the western U.S. coast, called Atmospheric Rivers

378 (ARs). ARs are typically associated with a low-level jet stream ahead of the cold front of  
379 extratropical cyclones (Zhu and Newell 1998; Dacre et al. 2015; Ralph et al. 2018), and  
380 can induce heavy precipitation where they make landfall and are forced to rise over  
381 mountain chains (Gimeno et al. 2014). The CAL event consists of a slow propagating  
382 surface front arching southeastward towards Oregon and then southwestward offshore  
383 of California (Figure 4a,c). Rain began over the coastal mountains of the Russian River  
384 watershed at 0700 UTC of February 16, as a warm front descended southward, and also  
385 coincided with the development of orographically favoured low-level upslope flow (Ralph  
386 et al., 2006).



388 **Figure 4: a,b) mean sea level pressure (mslp, white contour lines, hPa), surface**  
389 **temperature (color shading, °C) and 100-m wind direction (black arrows, m/s) at 0700 UTC,**  
390 **February 16, 2004 of ERA5 reanalysis and RegCM 12km respectively. c) NCEP-NOA**  
391 **Surface Analysis of pressure and fronts. The black box in c) bounded the area represented**  
392 **in a) and b)**

393 The intermediate resolution (12 km) domain (Figure 3a) covers a wide area  
394 encompassing California and a large portion of the coastal Pacific Ocean, with 23 vertical  
395 levels and a parameterization for deep convection based on the Kain–Fritsch scheme  
396 (Kain, 2004). The ERA-Interim driven simulation is initialized at 0000 UTC, February 15  
397 2004 (Table 2) and lasts until 0000 UTC February 19 2004. This simulation is used as a  
398 boundary conditions for a RegCM4-NH run over a smaller area centered over northern  
399 California (Fig. 3a) at 3 km horizontal resolution, with 41 vertical levels and boundary  
400 conditions updated every 6 hours. In RegCM4-NH only the shallow convection code of  
401 the Tiedtke scheme (Tiedtke, 1996) is activated. Simulated precipitation is compared with  
402 the CHIRPS, CMORPH, TRMM, PRISM, NCEP/CPC observations (Table 3).

403 As shown in Figure 4 the February 14 synoptic conditions for mean sea level pressure  
404 (mslp), surface temperature and wind direction of this case study, are well reproduced by  
405 RegCM4 at 12 km (Fig. 4b) when compared to ERA5 reanalysis (Fig. 4a). The surface  
406 analysis of pressure and fronts derived from the operational weather maps prepared at  
407 the National Centers for Environmental Prediction, Hydrometeorological Prediction  
408 Center, National Weather Service  
409 ([https://www.wpc.ncep.noaa.gov/dailywxmap/index\\_20040216.html](https://www.wpc.ncep.noaa.gov/dailywxmap/index_20040216.html)) is also reported in  
410 Figure 4c.

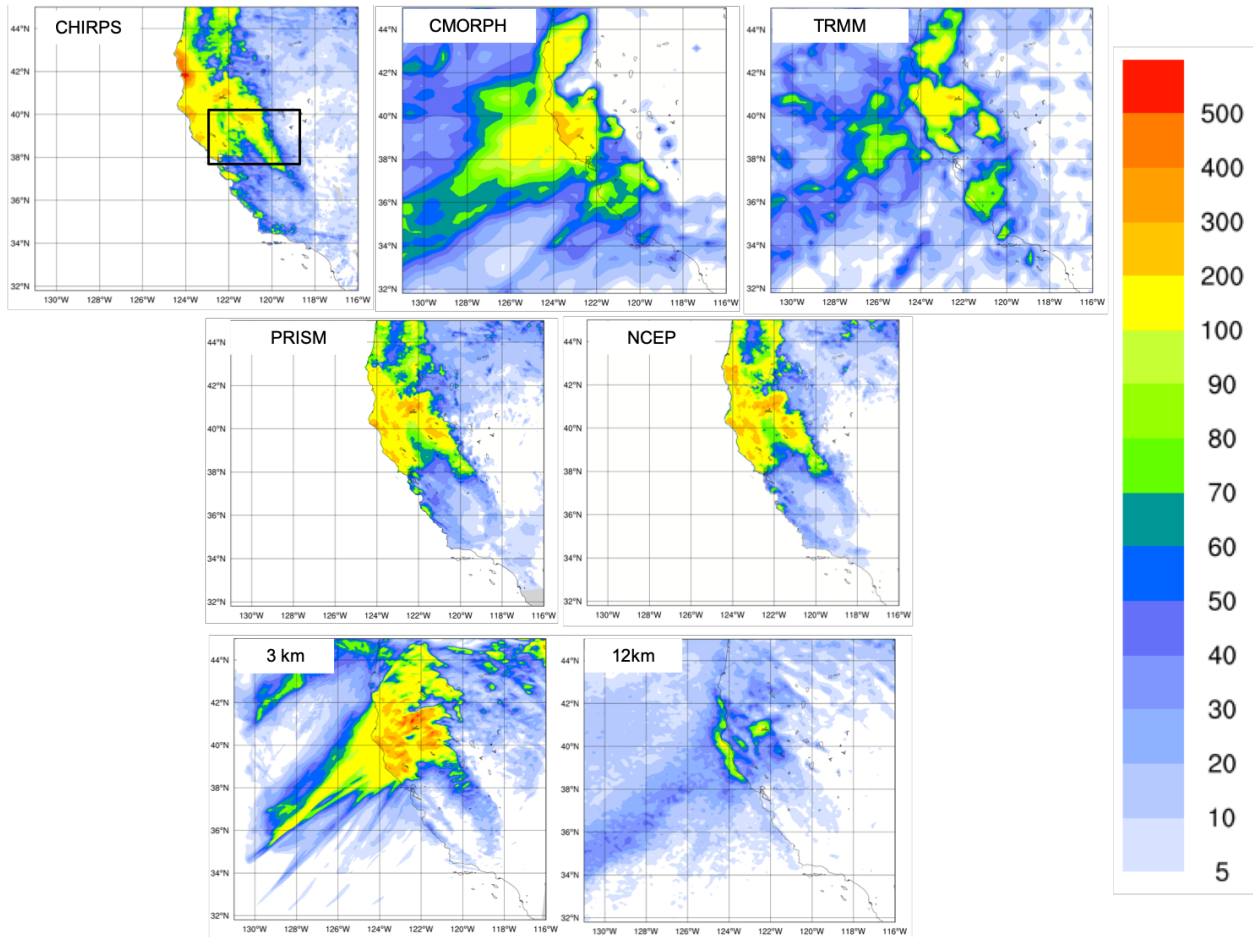
411 The available observed precipitation datasets show similar patterns for the total  
412 accumulated precipitation (Figure 5), in particular CHIRPS (Figure 5a), PRISM (Figure  
413 5d) and NCEP (Figure 5e) exhibit similar spatial details and magnitudes of extremes.  
414 CHIRPS shows a maximum around 42°N which is not found in the other datasets.  
415 CMORPH (Figure 5b) and TRMM (Figure 5c) show lower precipitation maxima and lesser  
416 spatial details due to their lower resolution, indicating that the performance of satellite-

417 based products may be insufficient as a stand alone product to validate the model for this  
418 case.

419 The largest observed maxima are placed on the terrain peaks, with extreme rainfall  
420 greater than 250 mm in 60 hours over the coastal mountains and between 100 – 175 mm  
421 elsewhere (Fig. 5). The black box in Fig 5a shows the area of the Russian River  
422 watershed where the largest rainfall rates were detected (269 mm and 124 mm in 60-h  
423 accumulated rainfall between 0000 UTC February 16 and 1200 UTC February 18, 2004,  
424 respectively) (Ralph et al., 2006).

425 The convection-permitting simulation captures the basic features of the observed  
426 precipitation, both in terms of spatial distribution (Fig. 5f) and of temporal evolution of  
427 rainfall (Fig. 6a). However, it shows higher precipitation rates than observed over the sea  
428 and over the mountain chains, with lower intensities than observed in the south-east part  
429 of the mountain chain (Fig. 5). The 12-km simulation instead severely underestimates the  
430 magnitude of the event (Fig. 5g).

431 Figure 6a shows the 6-hourly accumulated precipitation averaged over the black box in  
432 Figure 5a. The 3 km and 12 km simulations capture the onset of the event, but the peak  
433 intensity is strongly underestimated by the 12 km run, while it is well simulated by the 3  
434 km run, although the secondary maximum is overestimated. These results demonstrate  
435 that only the high resolution convection-permitting model is able to captures this extreme  
436 event, and that parameterized convection has severe limits in this regard (Done et al.  
437 2004; Lean et al. 2008; Weisman et al. 2008; Weusthoff et al. 2010; Schwartz 2014; Clark  
438 et al. 2016).



439

440 **Figure 5 : Total accumulated precipitation (mm) during the California case: CHIRPS (a),**  
 441 **CMORPH (b), TRMM (c) observations, PRISM (d) and NCEP Reanalysis (e) and convection-**  
 442 **permitting simulation with RegCM4-NH at 3km (f) and RegCM4 at 12km (g).The black box**  
 443 **denotes the area where the spatial average of 6-hourly accumulated precipitation is**  
 444 **calculated and reported in Fig. 6.**

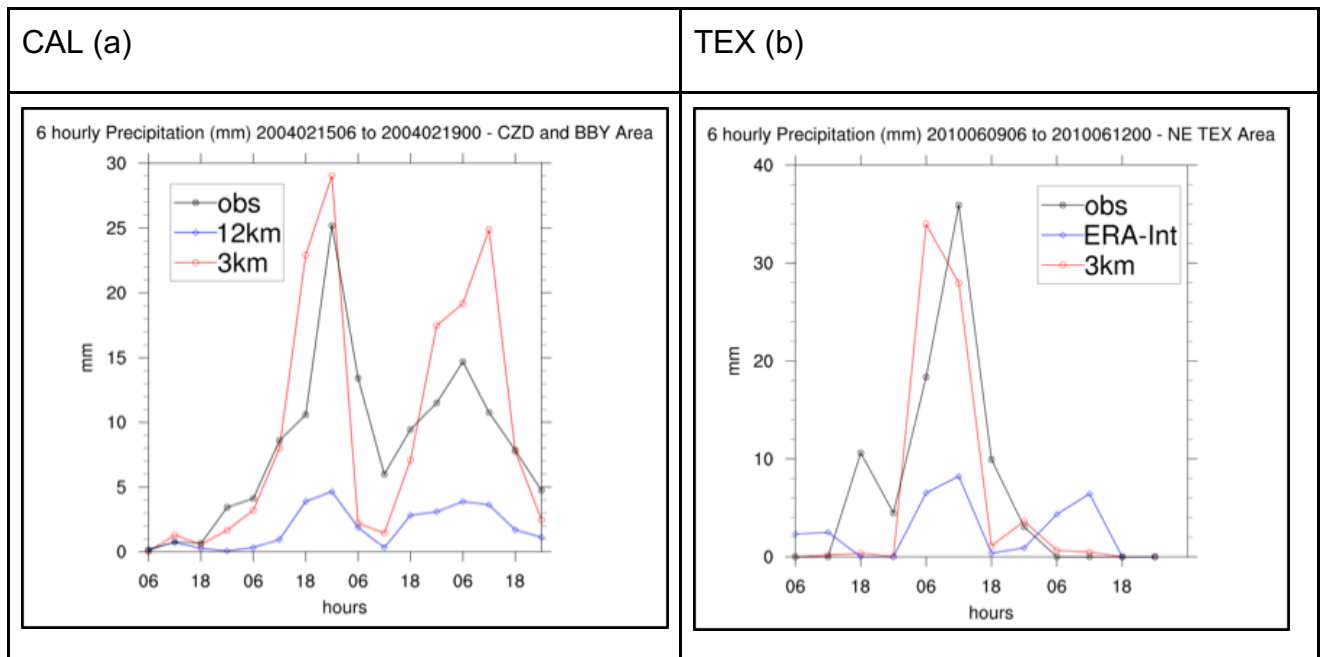
445

446

447

448

449



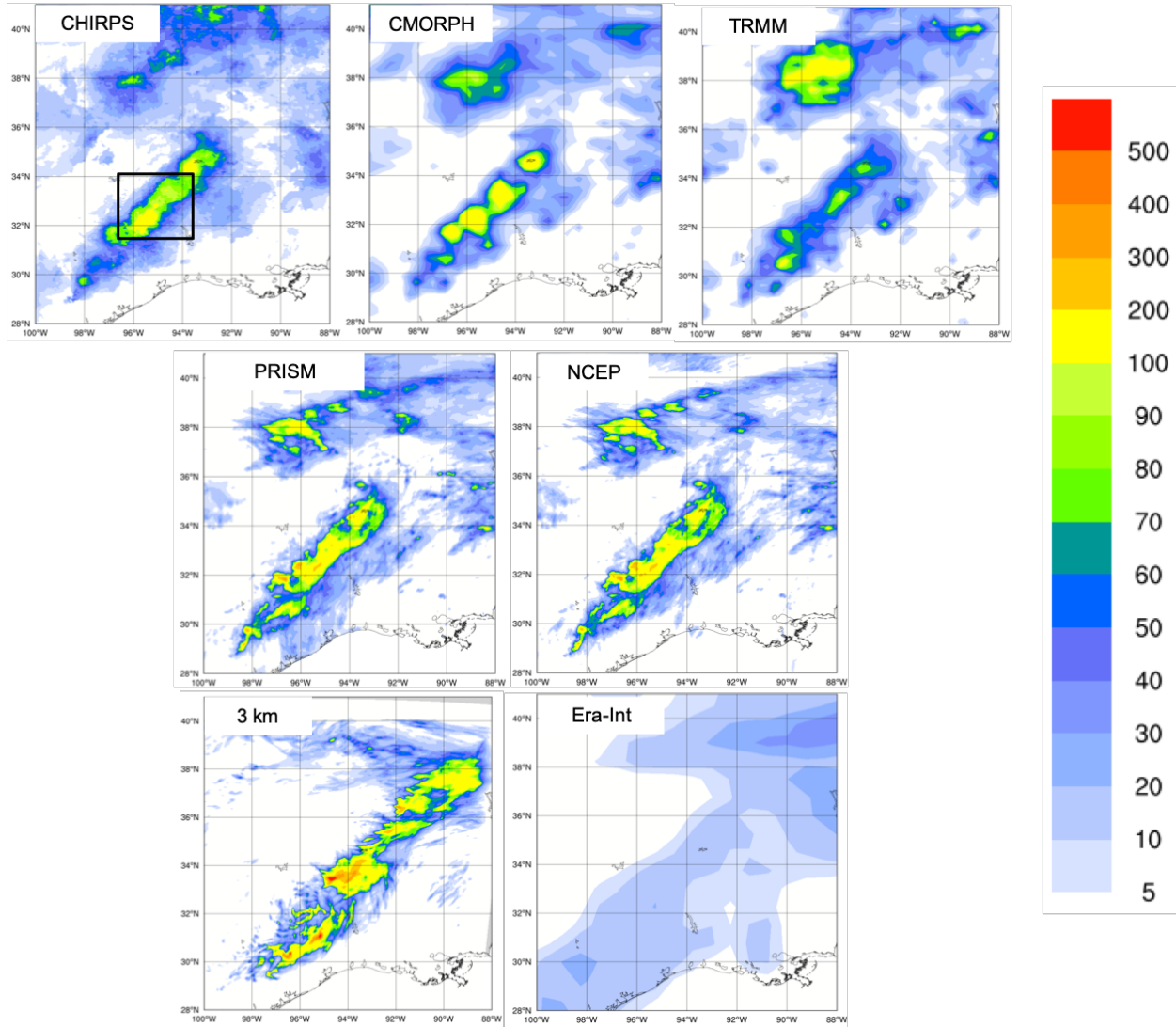
450 **Figure 6: Time series of the 6 hourly accumulated precipitation (in mm on the y-axis) during**  
 451 **the CAL event (a) and during the TEX event (b). The blue lines show RegCM4 12 Km and**  
 452 **ERA interim 6 hourly accumulated precipitation averaged over the areas indicated by the**  
 453 **black squares in Figures 5 and 7 while the red line shows the 6 hourly accumulated**  
 454 **precipitation simulated by RegCM4-NH. The observations are shown with a black line.**

455

456 **Texas**

457 Case 2, hereafter referred to as TEX (Table 2), is a convective precipitation episode  
 458 exhibiting characteristics of the “Maya Express” flood events, linking tropical moisture  
 459 plumes from the Caribbean and Gulf of Mexico to midlatitude flooding over the central  
 460 United States (Higgins 2011). During the TEX event, an upper-level cutoff low over  
 461 northeastern Texas, embedded within a synoptic-scale ridge, moved slowly  
 462 northeastward. Strong low-level flow and moisture transport from the western Gulf of  
 463 Mexico progressed northward across eastern Texas. The event was characterized by  
 464 low-level moisture convergence, weak upper-level flow, weak vertical wind shear, and  
 465 relatively cold air (center of cutoff low), which favored the slow-moving convective storms  
 466 and nearly stationary thunderstorm outflow boundaries. The main flooding event in

467 eastern Texas occurred on June 10, 2010, with a daily maximum rainfall of 216.4 mm for  
468 the region in the black box of Figure 7a (Higgins 2011).



469

470 **Figure 7: Total accumulated precipitation (mm) during the Texas case: CHIRPS (a),**  
471 **CMORPH (b), TRMM (c), PRISM (d), NCEP Reanalysis (e) and convection-permitting**  
472 **simulation with RegCM4-NH at 3 km grid spacing (f) and ERA-Interim (g).The black box (a)**  
473 **shows the area where the spatial average of 6-hourly accumulated precipitation was**  
474 **calculated and reported in Figure 6b**

475 As for the California case, the observed precipitation datasets show coherent patterns for  
476 the total accumulated precipitation (Figure 7), with the highest values related to the  
477 mesoscale convective system in eastern Texas (~ 200 mm), and another smaller area of



478 high precipitation more to the north, approximately over Oklahoma. PRISM (Figure  
479 7d) and NCEP (Figure 7e) capture similar spatial details and magnitudes of extremes,  
480 CHIRPS (Figure 7a) has lower precipitation extremes in the north compared to the other  
481 datasets, while CMORPH (Figure 7b) and TRMM (Figure 7c) show the lowest  
482 precipitation extremes and reduced spatial details as already noted for the California  
483 case.

484 Figure 7f and Figure 7g present precipitation as produced by the RegCM4-NH and the  
485 ERA-Interim reanalysis (driving data) respectively. ERA-Interim reproduces some of the  
486 observed features of precipitation, but with a substantial underestimation over the areas  
487 of maximum precipitation because of its coarse resolution. By comparison, the RegCM4-  
488 NH simulation (Fig. 7f) shows an improvement in both pattern and intensity of  
489 precipitation, and is substantially closer to observations over eastern Texas. However,  
490 the precipitation area is slightly overestimated and the model is not capable of  
491 reproducing the small region of maximum precipitation in the north.

492  
493 The time series of precipitation over eastern Texas from June 9 to 12, 2010 for  
494 observations (black line), ERA-Interim (blue line) and RegCM4-NH (red line) are reported  
495 in figure 6b. Precipitation increases over this region from 0000 UTC until it reaches the  
496 observed maximum at 1200 UTC, on June 10 (~35 mm), gradually decreasing afterwards  
497 until 0600 UTC, on June 11. The RegCM4-NH simulation shows a more realistic temporal  
498 evolution than the ERA-Interim, which exhibits an overall underestimation of precipitation.  
499 The non-hydrostatic model produces precipitation values closer to the observations,  
500 however the simulated maximum is reached 6 hours earlier than observed.

501

502

### 503 **Lake Victoria**

504 Case 3 focuses on Lake Victoria (LKV), with the purpose of testing RegCM4-NH on a  
505 complex and challenging region in terms of convective rainfall. It is estimated that each  
506 year 3,000-5,000 fishermen perish on the lake due to nightly storms (Red Cross, 2014).  
507 In the Lake Victoria basin, the diurnal cycle of convection is strongly influenced by  
508 lake/land breezes driven by the thermal gradient between the lake surface and the

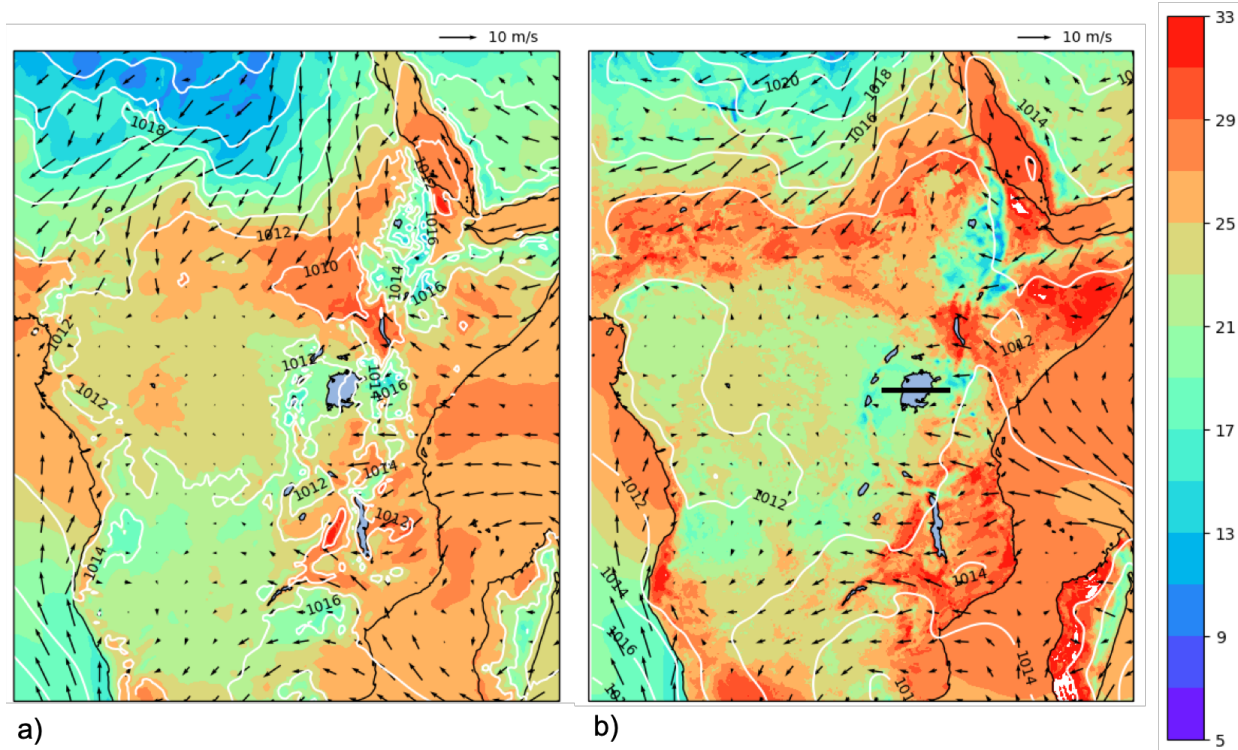
509 surrounding land. As the land warms during the course of the day, a lake breeze is  
510 generated which flows from the relatively cooler water towards the warmer land surface.  
511 The circulation is effectively reversed at night, when the land surface becomes cooler  
512 than the lake surface, leading to convergence over the lake and associated thermal  
513 instability.

514 In the LKV region, prevailing winds are generally easterly most of the year with some  
515 variability due to the movement of the ITCZ. The local diurnal circulation created by the  
516 presence of the lake creates two diurnal rainfall maxima. During daylight hours, when the  
517 lake breeze begins to advance inland, convergence is maximized on the eastern coast of  
518 the lake as the lake breeze interacts with the prevailing easterlies. Studies have also  
519 noted the importance of downslope katabatic winds along the mountains to the east of  
520 the lake in facilitating convergence along the eastern coastal regions (Anyah et al. 2006).  
521 This creates a maximum in rainfall and convection on the eastern coast of LKV.  
522 Conversely, during nighttime hours, when the local lake circulation switches to flow from  
523 the land towards the lake, the prevailing easterlies create locally strong easterly flow  
524 across the lake and an associated maximum in convergence and rainfall on the western  
525 side of LKV.

526 The LKV simulation starts on November 25, 1999 and extends to the beginning of  
527 December 1999 (Table 2), covering a 5-day period which falls within the short-rain season  
528 of East Africa. The choice of 1999, an ENSO neutral year, was made in order to focus the  
529 analysis on local effects, such as the diurnal convection cycle in response to the lake/land  
530 breeze, with no influence of anomalous large scale conditions. A 1-dimensional lake  
531 model (Hostetler et al. 1993; Bennington et al. 2014) interactively coupled to RegCM4-  
532 NH was utilized to calculate the lake surface temperature (LST), since lake-atmosphere  
533 coupling has been shown to be important for LKV (Sun et al. 2015; Song et al. 2004).  
534 This coupled lake model has been already used for other lakes, including Lake Malawi in  
535 southern Africa (Diallo et al. 2018). As with the other experiments, the boundary  
536 conditions are provided by a corresponding 12 km RegCM4 simulation employing the  
537 convection scheme of Tiedtke (1996).

538 At the beginning of the simulation, the LST over the lake is uniformly set to 26°C, and is  
539 then allowed to evolve according to the lake-atmosphere coupling. This initial LST value  
540 is based on previous studies. For example, Talling (1969) finds Lake Victoria surface  
541 temperatures ranging from 24.5-26°C during the course of the year. Several studies have  
542 used RCMs to investigate the Lake Victoria climate (Anyah et al., 2006; Anyah and  
543 Semazzi 2009, Sun et al. 2015), and found a significant relationship between lake  
544 temperature and rainfall depending on season. The value of 26°C is typical of the winter  
545 season and was chosen based on preliminary sensitivity tests using different values of  
546 initial temperature ranging from 24°C to 26°C.

547 The synoptic feature favorable for the production of precipitation over the LKV in this  
548 period corresponds to a large area of southeasterly flow from the Indian Ocean (Fig. 8a),  
549 which brings low-level warm moist air into the LKV region facilitating the production of  
550 convective instability and precipitation. This synoptic situation, with a low-level south-  
551 easterly jet off the Indian Ocean, is a common feature associated with high precipitation  
552 in the area (Anyah et al. 2006), and can be seen in ERA5 data (Figure 8a). Although  
553 some bias in terms of magnitude, this is reasonably well reproduced by the 12 km  
554 simulation (Figure 8b).



555 a) b)

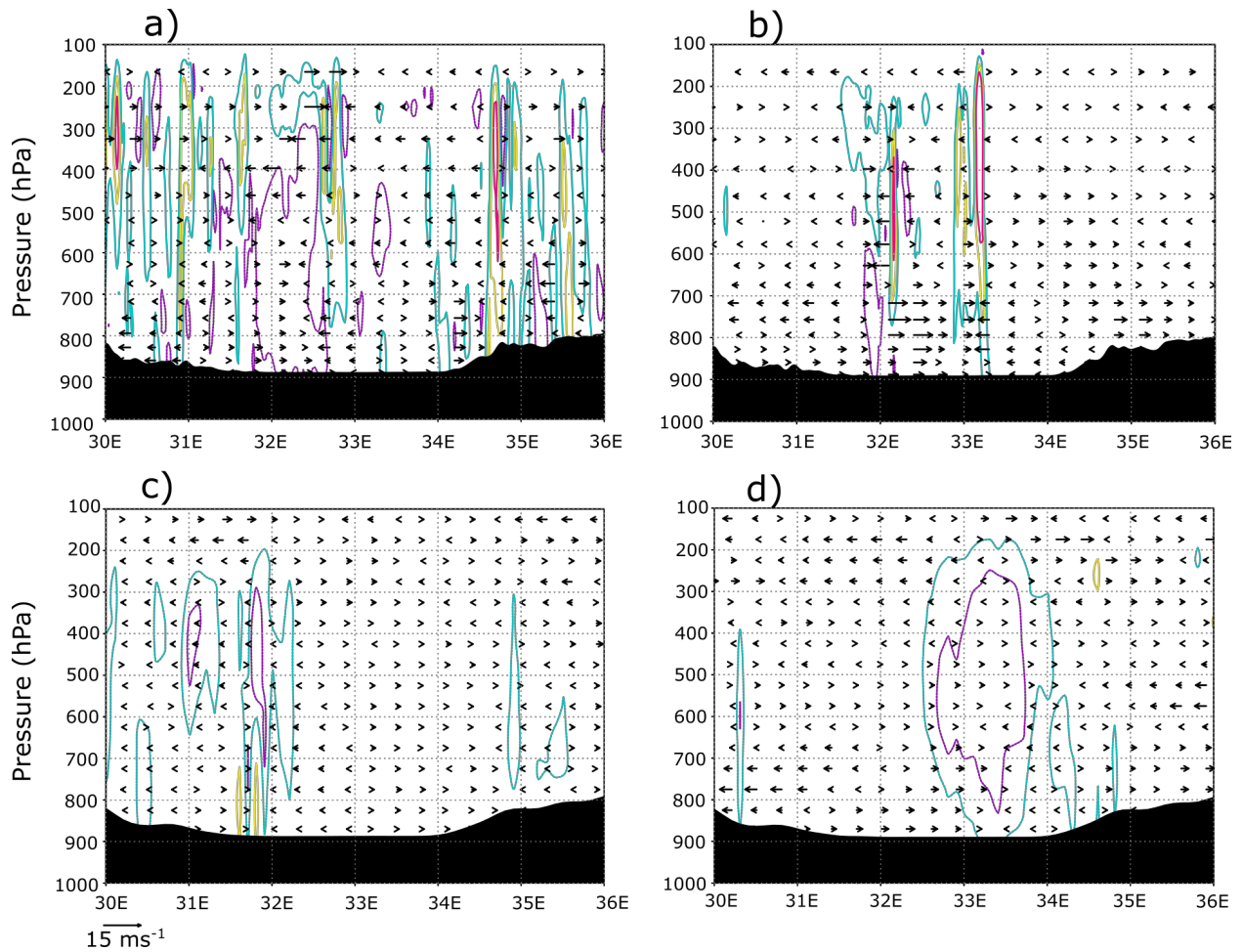
556 **Figure 8: Mean sea level pressure (mslp) (hPa) (white contour lines), surface temperature**  
 557 **(color shading) (°C) and 100-m wind (black arrows) averaged over the period 25 November**  
 558 **0000 UTC - 1 December 0000 UTC, by ERA5 reanalysis (a) and RegCM 12km (b). The black**  
 559 **line (b) shows the cross-section position represented in Fig. 9**

560 The LKV region dynamics are quite distinct between nighttime and daytime and the  
 561 rainfall in and around the lake has a pronounced diurnal cycle. To understand this strong  
 562 diurnal cycle, Figure 9 shows a cross-section through the lake (32°E to 34°E, black line  
 563 in right panel of Fig. 8b) along 1°S latitude at a period during strong nighttime (Fig. 9b,d;  
 564 0600Z November 30) and daytime convection (Figure 9a,c; 12Z November 29). Wind  
 565 vectors in Figure 9 show the zonal-wind anomaly across 0°-2°S to highlight the  
 566 circulations associated with LKV. During the day, surface heating around the lake leads  
 567 to a temperature difference between the land and lake sufficient to generate a lake  
 568 breeze, which causes divergence over the lake, while over the highlands to the east the  
 569 environment is more conducive to convection where convergence is focused (9a,c).  
 570 Conversely, during the night, a land breeze circulation is generated, which induces  
 571 convergence and convection over the lake (Figure 9b,d). In Figure 10, the evolution of

572 the nighttime land breeze is illustrated with cooler temperature anomalies propagating  
573 westward onto the lake during the night.

574 Comparing the 3 km simulation to the 12 km forcing run, we find that the localized  
575 circulations created by local forcings (i.e. convection) are much stronger in the convection  
576 permitting resolution experiment. We also find stronger and more localized areas of  
577 convective updrafts compared to the 12 km simulation (Figure 9c,d; omega is shown  
578 instead of vertical velocity here because of the difference in dynamical core). As an  
579 example during the nighttime event (Figure 9b,d) there is a broad area of upward motion  
580 over the lake and the associated broad convergence in the 12km simulation, while in the  
581 convection permitting 3km simulation, convection is much more local and concentrated  
582 over the western part of the lake. Indeed, nighttime rainfall tends to be concentrated over  
583 the western part of the lake ( Sun et al. 2015; Figure 11a-d). Stronger convection  
584 simulated in the 3 km experiment could also be tied to stronger temperature anomalies  
585 shown over the lake and land and between day and night relative to the 12km simulation  
586 (Figure 10). The 3km simulation also shows a more pronounced land breeze propagation  
587 at night compared to the 12km simulation.

588 This demonstrates that the 3km simulation is better equipped to simulate the localized  
589 circulations associated with this complex land-lake system.

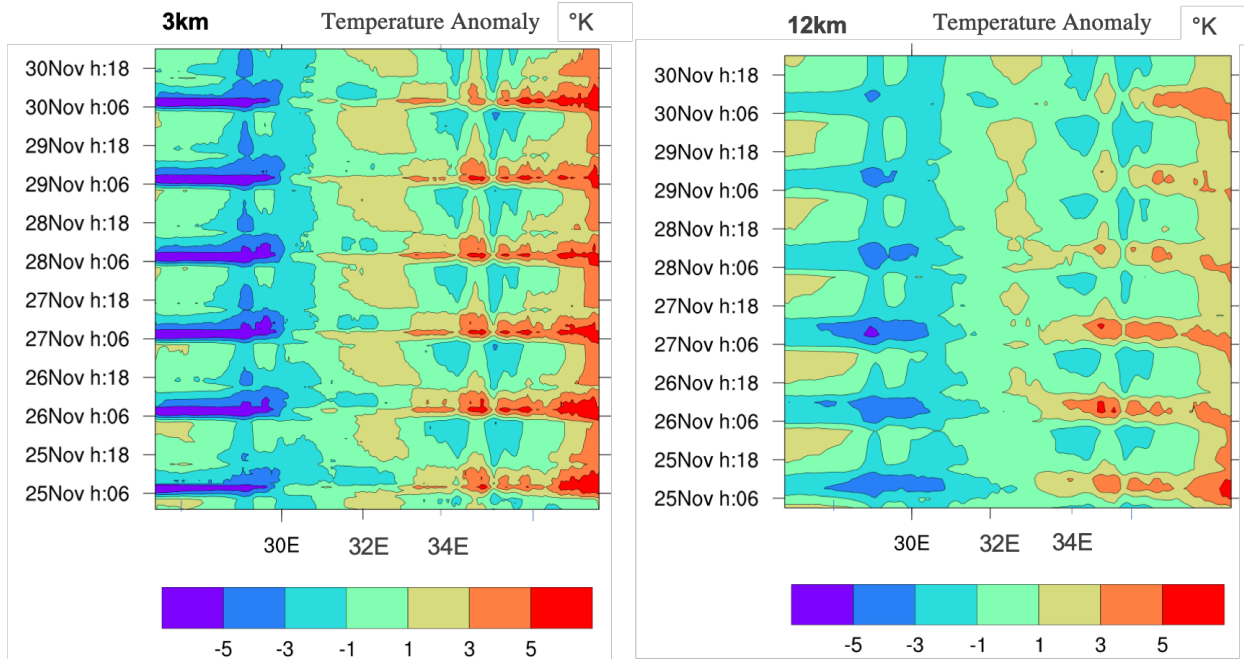


590

591

592 **Figure 9. Cross-section through 1°S (black line in Fig. 8b) of the zonal-wind anomaly (0o-**  
 593 **2oS) vectors and the mean contoured vertical velocity (m/s) over 0°-2°S at a) 12Z 29**  
 594 **November and b) 6Z 30 November from the 3km simulation. Purple dashed contours**  
 595 **indicate -0.1 m/s, light blue contours indicate 0.1 m/s, yellow contours indicate 0.3 m/s,**  
 596 **and red contours indicate 0.5 m/s. Lake Victoria encompasses about 32°E to 34°E. The**  
 597 **bottom 2 panels show the same as in a) and b) but from the 12km simulation at c) 12Z 29**  
 598 **November and d) 6Z 30 November. Purple dashed contours indicate -0.01 hPa/s, light blue**  
 599 **dashed contours indicate -0.005 hPa/s, and yellow dashed contours indicate 0.005 hPa/s.**

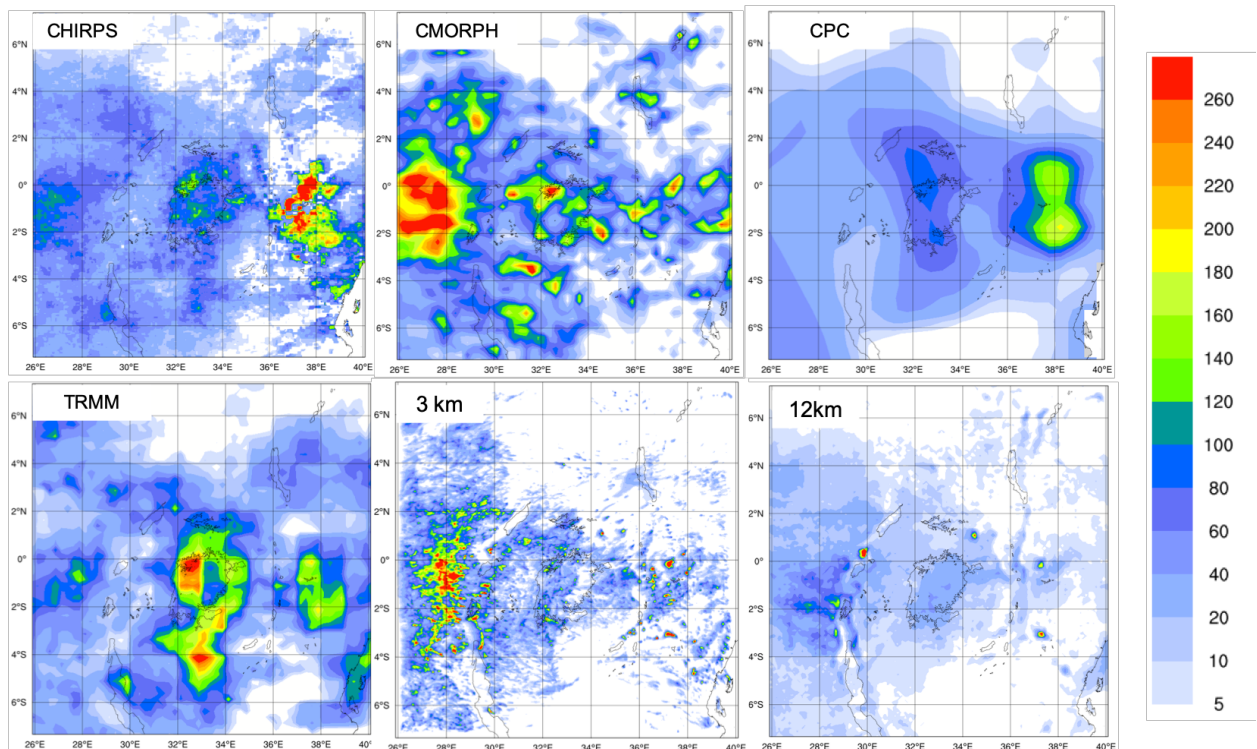
600



601

602 **Figure 10 : Longitude-time (hourly) Hovmöller diagram of LKV domain surface temperature**  
 603 **anomaly (shading, in °K). Panels correspond to the 3km simulation (left) and 12km**  
 604 **simulation (right). The lake Victoria is between 32°E and 34°E longitude**

605



606

607 **Figure 11: Total event accumulated precipitation (mm) during the LKV case (November 25,**  
 608 **1999-December 1, 1999) measured by CHIRPS (a ), CMORPH (b ), CPC (d) TRMM (e ) and**  
 609 **calculated by RegCM4 at 3 km (e ) and 12 km (f ).**

610

611 Figure 11 reports the total accumulated precipitation observed and simulated for the LKV  
 612 case. TRMM (Figure 11d) and CPC (Figure 11c) show a similar pattern, with two-rainfall  
 613 maxima of different intensities over the southeastern and northwestern lake areas.  
 614 CMORPH (Figure 11b) shows a western rainfall maximum similar to TRMM and one large  
 615 rainfall area almost entirely centered over the highlands to the west of the lake.  
 616 Conversely in CHIRPS (Figure 11a) a maximum is found to the east of the lake while  
 617 several localized maxima occur over the lake. The differences among the observed  
 618 datasets highlight the issue of observational uncertainty and the need to take into  
 619 consideration shortcomings associated with the types of observational datasets  
 620 considered. Different datasets can have significantly different climatologies, especially in  
 621 areas of low data availability. For example, Prein and Gobiet (2017) analyzed two gauge-  
 622 based European-wide datasets, and seven global low-resolution datasets, and found



623 large differences across the observation products, often of similar magnitude as the  
624 difference among model simulations. In this case and for this area the observation  
625 uncertainty plays a big role especially at high resolution, and highlights the need for an  
626 adequate observational network for model validation. However, despite the large  
627 uncertainty among the different observed datasets (Figure 11 a-d), we find a significant  
628 underestimation of the precipitation by the 12 km run over the lake independently of the  
629 dataset used as a reference (Figure 11f). In contrast, the 3 km simulation (Figure 11e)  
630 shows substantially greater detail, with rainfall patterns more in agreement with the  
631 CMORPH data. In particular, the 3 km simulation reproduces well the local rainfall  
632 maxima on the western side of the lake, although these appear more localized and with  
633 a multi-cell structure compared to CMORPH and TRMM. Additionally, the 12 km  
634 simulation underestimates the observed heavy rainfall totals in the highlands to the west  
635 of the lake region especially when compared to CMORPH, which are instead reproduced  
636 by the 3 km simulation.

637 This last test case demonstrates the ability of RegCM4-NH in simulating realistic  
638 convective activity over a such morphologically complex region, which is a significant  
639 improvement compared to the hydrostatic-coarse resolution model configuration.

640

## 641 **Conclusions and future outlook**

642

643 In this paper we have described the development of RegCM4-NH, a non hydrostatic  
644 version of the regional model system RegCM4, which was completed in response to the  
645 need of moving to simulations at convection-permitting resolutions of a few kilometers.  
646 The non-hydrostatic dynamical core of MM5 has been incorporated into the RegCM4  
647 system previously based on the MM5 hydrostatic core. Some modifications to the MM5  
648 dynamical core were also implemented to increase the model stability for long term runs.  
649 RegCM4-NH also includes two explicit cloud microphysics schemes needed to explicitly  
650 describe convection and cloud processes in the absence of the use of cumulus  
651 convection schemes. Finally, we presented a few case studies of explosive convection to

652 illustrate how the model provides realistic results in different settings and general  
653 improvements compared to the coarser resolution hydrostatic version of RegCM4 for  
654 such types of events.

655  
656 As already mentioned, RegCM4-NH is currently being used for different projects, and  
657 within these contexts, is being run at grid spacings of a few kilometers for continuous  
658 decadal simulations, driven by reanalyses of observations or GCM boundary conditions  
659 (with the use of an intermediate resolution domains) over different regions, such as the  
660 Alps, the Eastern Mediterranean, Central-Eastern Europe and the Caribbeans. These  
661 projects, involving multi-model intercomparisons, indicate that the performance of  
662 RegCM4-NH is generally in line with that of other convection-permitting models, and  
663 exhibits similar improvements compared to coarser resolution models, such as a better  
664 simulation of the precipitation diurnal cycle and of extremes at hourly to daily time scales.  
665 The results obtained within the multi-model context confirm previous results from single-  
666 model studies (Kendon et al. 2012, 2017, Ban et al. 2014, 2015; Prein et al. 2015, 2017),  
667 but also strengthen the robustness of the findings through reduced uncertainty compared  
668 to coarse resolution counterpart (Ban et al., 2021, Pichelli et al., 2021). The convection-  
669 permitting scale can thus open the perspective of more robust projections of future  
670 changes of precipitation, especially over sub-daily time scales.

671  
672 One of the problems of the RegCM4-NH dynamical core is that, especially for long runs  
673 with varied meteorological conditions, a relatively short time step is needed for stability  
674 reasons. This makes the model rather computationally demanding, although not more  
675 than other convection-permitting modeling systems such as the Weather Research and  
676 Forecast model (WRF, Skamarok et al. 2008). For this reason, we are currently  
677 incorporating within the RegCM system a very different and more computationally efficient  
678 non-hydrostatic dynamical core, which will provide the basis for the next version of the  
679 model, RegCM5, to be released in the future.

680  
681 Following the philosophy of the RegCM modeling system, RegCM4-NH is intended to be  
682 a public, free, open source community resource for external model users. The non-

683 hydrostatic dynamical core has been implemented in a way that it can be activated in  
684 place of the hydrostatic dynamics through a user-set switch, which makes the use of  
685 RegCM4-NH particularly simple and flexible. We therefore envision that the model will be  
686 increasingly used by a broad community so that a better understanding can be achieved  
687 of its behavior, advantages and limitations.

688

689 **Code availability:** <https://zenodo.org/record/4603556>

690 **Cases study configuration files:** <https://zenodo.org/record/5106399>

691

692

693 **Author contribution:** CE prepared the manuscript with contributions from all co-authors  
694 and coordinated research, SP, TA, GR carried out and analysed the simulations, PE  
695 investigated solutions to stabilize/adapt the model at the km-scale and performed  
696 preliminary validation tests, GG developed/adapted the model code, FDS contributed to  
697 develop the coupled version of the model, NR developed one of the microphysics  
698 scheme, GF supervised and coordinated all activities.

699

700 **Competing interests:** The authors declare that they have no conflict of interest.

701

702

## 703 References

704 Anyah, R., Semazzi, F. H. M., Xie, L., 2006: Simulated Physical Mechanisms Associated  
705 with Climate Variability over Lake Victoria Basin in East Africa, *Mon. Wea. Rev.*, 134  
706 3588-3609.

707

708 Anthes, R. A., Hsie, E. -Y., & Kuo, Y. -H. (1987). Description of the Penn State/NCAR  
709 Mesoscale Model: Version 4 (MM4) (No. NCAR/TN-282+STR). doi:10.5065/D64B2Z90

710

711 Anyah, R. O., F. H. M. Semazzi, L. Xie, 2006: Simulated Physical Mechanisms  
712 Associated with Climate Variability over Lake Victoria Basin in East Africa. *Mon. Wea.*  
713 *Rev.*, 134, 3588-3609,.

714

715 Anyah RO, Semazzi F (2009) Idealized simulation of hydrodynamic characteristics of  
716 Lake Victoria that potentially modulate regional climate. *Int J Climatol* 29(7):971–981.  
717 doi:[10.1002/joc.1795](https://doi.org/10.1002/joc.1795)

718

719 Ashouri, Hamed, Kuo Lin Hsu, Soroosh Sorooshian, Dan K. Braithwaite, Kenneth R.  
720 Knapp, L. Dewayne Cecil, Brian R. Nelson and Olivier P. Prat (2015). 'PERSIANN- CDR:  
721 Daily precipitation climate data record from multisatellite observations for hydrological and  
722 climate studies'. In: *Bulletin of the American Meteorological Society*. ISSN: 00030007.  
723 DOI: 10.1175/BAMS-D-13-00068.1.

724

725 Ban, N., J. Schmidli, and C. Schär, 2014: Evaluation of the convection-resolving regional  
726 climate modeling approach in decade-long simulations. *J. Geophys. Res. Atmos.*, 119,  
727 7889– 7907, <https://doi.org/10.1002/2014JD021478>.

728

729 Ban N, Schmidli J, Schär C (2015) Heavy precipitation in a changing climate: does short-  
730 term summer precipitation increase faster? *Geophys Res Lett* 42:1165–1172.  
731 <https://doi.org/10.1002/2014GL062588>

732 Ban, N., Caillaud, C., Coppola, E. *et al.* The first multi-model ensemble of regional climate  
733 simulations at kilometer-scale resolution, part I: evaluation of precipitation. *Clim Dyn*  
734 (2021). <https://doi.org/10.1007/s00382-021-05708-w>

735

736 Beheng, K.: A parameterization of warm cloud microphysical conversion processes,  
737 *Atmos. Res.*, 33, 193–206, 1994

738

739 Bennington V, Notaro M, Holman KD, 2014: Improving Climate Sensitivity of Deep Lakes  
740 within a Regional Climate Model and Its Impact on Simulated Climate, *J. Clim*, 27, 2886-  
741 2911.

742

743 Bretherton CS, McCaa JR, Grenier H (2004) A new parameterization for shallow cumulus  
744 convection and its application to marine subtropical cloud-topped boundary layers. I.  
745 Description and 1D results. *Mon Weather Rev* 132: 864– 882  
746

747 Chan, S. C., E. J. Kendon, H. J. Fowler, S. Blenkinsop, N. M. Roberts, and C. A. T. Ferro,  
748 2014: The value of high-resolution Met Office regional climate models in the simulation  
749 of multi-hourly precipitation extremes. *J. Climate*, 27, 6155–6174,  
750 <https://doi.org/10.1175/JCLI-D-13-00723.1>.  
751

752 Chen, Mingyue and Pingping Xie (2008). 'CPC Unified Gauge-based Analysis of Global  
753 Daily Precipitation'. In: *2008 Western Pacific Geophysics Meeting*. ISBN: 0026- 0576.  
754 DOI: [http://dx.doi.org/10.1016/S0026-0576\(07\)80022-5](http://dx.doi.org/10.1016/S0026-0576(07)80022-5).  
755

756

757 Clark, P., N. Roberts, H. Lean, S. P. Ballard, and C. Charlton-Perez, 2016: Convection-  
758 permitting models: A step-change in rainfall forecasting. *Meteor. Appl.*, 23, 165–181,  
759 <https://doi.org/10.1002/met.1538>.  
760

761 Coppola, E., Sobolowski, S., Pichelli, E. et al. A first-of-its-kind multi-model convection  
762 permitting ensemble for investigating convective phenomena over Europe and the  
763 Mediterranean. *Clim Dyn* 55, 3–34 (2020). <https://doi.org/10.1007/s00382-018-4521-8>  
764

765 Coppola E, Giorgi F, Mariotti L, Bi X (2012) RegT-Band: a tropical band version of  
766 RegCM4. *Clim Res* 52: 115–133  
767

768 Dacre, H. F., P. A. Clark, O. Martinez-Alvarado, M. A. Stringer, and D. A. Lavers, 2015:  
769 How do atmospheric rivers form? *Bull. Amer. Meteor. Soc.*, 96, 1243-1255,  
770 <https://doi.org/10.1175/BAMS-D-14-00031>.  
771

772 Dale, M., A. Hosking, E. Gill, E. J. Kendon, H. J. Fowler, S. Blenkinsop, and S. C. Chan,  
2018: Understanding how changing rainfall may impact on urban drainage systems; les-

773 sons from projects in the UK and USA. *Water Pract. Technol.*, 13, 654–661,  
774 <https://doi.org/10.2166/wpt.2018.069>.

775

776 Diallo, I., Giorgi, F. and Stordal, F. (2018) Influence of Lake Malawi on regional climate  
777 from a double nested regional climate model experiment. *Climate Dynamics*, 50, 3397–  
778 3411. <https://doi.org/10.1007/s00382-017-3811-x>

779

780 Dickinson, R.E., Errico, R.M., Giorgi, F. et al. A regional climate model for the western  
781 United States. *Climatic Change* 15, 383–422 (1989). <https://doi.org/10.1007/BF00240465>

782

783 Dickinson RE, Henderson-Sellers A, Kennedy P (1993) Bio -sphere– atmosphere transfer  
784 scheme (BATS) version 1eas coupled to the NCAR community climate model. TechRep,  
785 National Center for Atmospheric Research TechNote NCAR.TN-387+ STR, NCAR,  
786 Boulder, CO

787

788 Done, J., C. A. Davis, and M. L. Weisman, 2004: The next gener- ation of NWP: Explicit  
789 forecasts of convection using the Weather Research and Forecasting (WRF) model.  
790 *Atmos. Sci. Lett.*, 5, 110–117, <https://doi.org/10.1002/asl.72>.

791

792 Dudhia, J., 1989: Numerical study of convection observed during the winter monsoon  
793 experiment using a mesoscale two-dimensional model, *J. Atmos. Sci.*, 46, 3077–3107.

794

795 Durran D.R. and Klemp J.B.: A compressible model for the simulation of moist mountain  
796 waves, *Mon. Wea. Rev.*, 111, 2341–236, 1983.

797

798 Elguindi N., Bi X., Giorgi F. , Nagarajan, B. Pal J., Solmon F., Rauscher S., Zakey S.,  
799 O'Brien T., Nogherotto R. and Giuliani G., 2017: Regional Climate Model  
800 RegCMReference ManualVersion 4.7, 49 pp, <https://zenodo.org/record/4603616>

801

802 Emanuel KA (1991) A scheme for representing cumulus convection in large-scale  
803 models. *J Atmos Sci* 48:2313–2335

804

805 Fairall, C.W., E.F. Bradley, J.S. Godfrey, G.A. Wick, J.B. Edson, and G.S. Young, 1996a:  
806 The cool skin and the warm layer in bulk flux calculations. *J. Geophys. Res.* 101, 1295-  
807 1308.

808

809 Fairall, C.W., E.F. Bradley, D.P. Rogers, J.B. Edson, G.S. Young, 1996b: Bulk  
810 parameterization of air-sea fluxes for TOGA COARE. *J. Geophys. Res.* 101, 3747-3764

811

812 Funk, C., Peterson, P., Landsfeld, M. et al. The climate hazards infrared precipitation with  
813 stations—a new environmental record for monitoring extremes. *Sci Data* 2, 150066  
814 (2015). <https://doi.org/10.1038/sdata.2015.66>

815

816 Gimeno, L., R. Nieto, M. Vázquez, and D. A. Lavers, 2014: Atmospheric rivers: A mini-  
817 review. *Front. Earth Sci.*, 2, <https://doi.org/10.3389/feart.2014.00002>.

818

819 Giorgi F (2019) Thirty years of regional climate modeling: where are we and where are  
820 we going next? *J Geophys Res Atmos* 124:5696–5723

821

822 Giorgi F, Coppola E, Solmon F, Mariotti L and others (2012) RegCM4: model description  
823 and preliminary tests over multiple CORDEX domains. *Clim Res* 52:7-29.  
824 <https://doi.org/10.3354/cr01018>

825

826

827

828 Giorgi F, Francisco R, Pal JS (2003) Effects of a sub-gridscale topography and landuse  
829 scheme on surface climate and hydrology. I. Effects of temperature and water  
830 vapor disaggregation. *J Hydrometeorol* 4: 317– 333

831

832 Giorgi F, Jones C, Asrar G (2009) Addressing climate information needs at the regional  
833 level: the CORDEX framework. *WMO Bull* 175–183

834

835 Giorgi F, Mearns LO (1999) Introduction to special section: regional climate modeling  
836 revisited. *J Geophys Res* 104:6335–6352  
837

838 Giorgi F, Marinucci MR, Bates G (1993a) Development of a second generation regional  
839 climate model (RegCM2). I. Boundary layer and radiative transfer processes.  
840 *MonWeather Rev* 121: 2794–2813  
841

842 Giorgi F, Marinucci MR, Bates G, DeCanio G (1993b) Development of a second  
843 generation regional climate model (RegCM2), part II: convective processes and  
844 assimilation of lateral boundary conditions. *Mon Weather Rev* 121:2814–2832  
845

846 Giorgi, F., and G. T. Bates, 1989: The Climatological Skill of a Regional Model over  
847 Complex Terrain. *Mon. Wea. Rev.*, 117, 2325–2347, [https://doi.org/10.1175/1520-0493\(1989\)117<2325:TCSOAR>2.0.CO;2](https://doi.org/10.1175/1520-0493(1989)117<2325:TCSOAR>2.0.CO;2).  
848

849 G. A. Grell, J. Dudhia and D. R. Stauffer, “A Description of the Fifth Generation Penn  
850 State/NCAR Mesoscale Model (MM5),” NCAR Tech. Note, NCAR/TN-398+ STR,  
851 Boulder, 1995, p. 122.  
852

853 Grell GA (1993) Prognostic evaluation of assumptions used by cumulus  
854 parameterizations. *Mon Weather Rev* 121: 764– 787  
855

856 Grell, G., A.J. Dudhia, and D.R. Stauffer, 1994, A description of the fifth-generation Penn  
857 State/NCAR mesoscale model (MM5). NCAR Technical Note, NCAR/TN- 398+STR.  
858

859 Gunn, K. L. S., and J. S. Marshall, 1958: The distribution with size of aggregate  
860 snowflakes. *J. Meteor.*, 15, 452–461, [https://doi.org/10.1175/1520-0469\(1958\)015<0452:TDWSOA>2.0.CO;2](https://doi.org/10.1175/1520-0469(1958)015<0452:TDWSOA>2.0.CO;2).  
861  
862

863 Gutowski Jr., W. J., Giorgi, F., Timbal, B., Frigon, A., Jacob, D., Kang, H.-S., Raghavan,  
864 K., Lee, B., Lennard, C., Nikulin, G., O'Rourke, E., Rixen, M., Solman, S., Stephenson,  
865 T., and Tangang, F.: WCRP COordinated Regional Downscaling EXperiment (CORDEX):



866 a diagnostic MIP for CMIP6, *Geosci. Model Dev.*, 9, 4087–4095,  
867 <https://doi.org/10.5194/gmd-9-4087-2016>, 2016

868  
869 Holtslag A, de Bruijn E, Pan HL (1990) A high resolution air mass transformation model  
870 for short-range weather fore-casting. *Mon Weather Rev* 118: 1561–1575

871  
872 Hostetler SW, Bates GT, Giorgi F (1993) Interactive nesting of a lake thermal model within  
873 a regional climate model for climate change studies. *J Geophys Res* 98: 5045– 5057

874  
875 Huffman, G. J., and Coauthors, 2007: The TRMM Multisatellite Precipitation Analysis  
876 (TMPA): Quasi-global, multiyear, combined-sensor precipitation estimates at fine scales.  
877 *J. Hydrometeor.*, 8, 38–55, doi:<https://doi.org/10.1175/JHM560.1>

878  
879 Kiehl J, Hack J, Bonan G, Boville B, Breigleb B, WilliamsonD, Rasch P (1996)  
880 Description of the NCAR Community Climate Model (CCM3). National Center for  
881 Atmospheric Research Tech Note NCAR/TN-420+ STR, NCAR, Boulder, CO

882  
883 Lean, H. W., P. A. Clark, M. Dixon, N. M. Roberts, A. Fitch, R. Forbes, and C. Halliwell,  
884 2008: Characteristics of high- resolution versions of the Met Office Unified Model for  
885 forecasting convection over the United Kingdom. *Mon. Wea. Rev.*, 136, 3408–3424,  
886 <https://doi.org/10.1175/2008MWR2332.1>.

887  
888 Lind, P., D. Lindstedt, E. Kjellstrom, and C. Jones, 2016: Spatial and temporal  
889 characteristics of summer precipitation over central Europe in a suite of high-resolution  
890 climate models. *J. Climate*, 29, 3501–3518, <https://doi.org/10.1175/JCLI-D-15-0463.1>.

891  
892 Hewitt, C. D., and J. A. Lowe, 2018: Toward a European climate prediction system. *Bull.*  
893 *Amer. Meteor. Soc.*, 99, 1997–2001, <https://doi.org/10.1175/BAMS-D-18-0022.1>.

894 Hong, S.-Y., H.-M. H. Juang, and Q. Zhao, 1998: Implementation of prognostic cloud  
895 scheme for a regional spectral model, *Mon. Wea. Rev.*, 126, 2621–2639.

896

897 Hong, S.-Y., J. Dudhia, and S.-H. Chen, 2004: A Revised Approach to Ice Microphysical  
898 Processes for the Bulk Parameterization of Clouds and Precipitation, *Mon. Wea. Rev.*,  
899 132, 103–120.

900

901 Hong, S.-Y., and J.-O. J. Lim, 2006: The WRF Single-Moment 6-Class Microphysics  
902 Scheme (WSM6), *J. Korean Meteor. Soc.*, 42, 129–151

903

904 Hostetler SW, Bates GT, Giorgi F, 1993: Interactive Coupling of Lake Thermal Model with  
905 a Regional climate Model, *J. Geophys. Res.*, 98(D3), 5045-5057.

906

907 Huffman, George J., David T. Bolvin, Eric J. Nelkin, David B. Wolff, Robert F. Adler,  
908 Guojun Gu, Yang Hong, Kenneth P. Bowman and Erich F. Stocker (2007). *The TRMM*  
909 *Multisatellite Precipitation Analysis (TMPA): Quasi-Global, Multiyear, Combined-Sensor*  
910 *Precipitation Estimates at Fine Scales*. DOI: 10.1175/JHM560.1.

911

912 Joyce, Robert J., John E. Janowiak, Phillip A. Arkin, Pingping Xie, 2004: CMORPH: A  
913 Method that Produces Global Precipitation Estimates from Passive Microwave and  
914 Infrared Data at High Spatial and Temporal Resolution. *J. Hydrometeor*, 5, 487–503

915

916 Kain, J. S., 2004: The Kain–Fritsch convective parameterization: An update. *J. Appl.*  
917 *Meteor.*, 43, 170–181, [https://doi.org/10.1175/1520-](https://doi.org/10.1175/1520-0450(2004)043<0170:TKCPAU>2.0.CO;2)  
918 [0450\(2004\)043](https://doi.org/10.1175/1520-0450(2004)043<0170:TKCPAU>2.0.CO;2)<0170:TKCPAU>2.0.CO;2.

919

920 Kain, J. S., and J. M. Fritsch, 1990: A one-dimensional entraining/ detraining plume model  
921 and its application in convective parameterization, *J. Atmos. Sci.*, 47, 2784–2802.

922

923 Kendon, E. J., N. M. Roberts, C. A. Senior, and M. J. Roberts, 2012: Realism of rainfall  
924 in a very high-resolution regional climate model. *J. Climate*, 25, 5791–5806,  
925 [https://doi.org/ 10.1175/JCLI-D-11-00562.1](https://doi.org/10.1175/JCLI-D-11-00562.1).

926

927 Kendon, E. J., and Coauthors, 2017: Do convection-permitting regional climate models  
928 improve projections of future precipitation change? *Bull. Amer. Meteor. Soc.*, 98, 79–93,  
929 [https://doi.org/ 10.1175/BAMS-D-15-0004.1](https://doi.org/10.1175/BAMS-D-15-0004.1)  
930

931 Kessler, E., 1969: On the Distribution and Continuity of Water Substance in Atmospheric  
932 Circulations. *Meteor. Monogr.*, No. 32, Amer. Meteor. Soc., 84 pp.  
933

934 Khairoutdinov, M. and Kogan, Y.: A new cloud physics parameterization in a large-eddy  
935 simulation model of marine stratocumulus, *B. Am. Meteorol. Soc.*, 128, 229–243, 2000  
936

937 Klemp, J.B. and Dudhia, J.: An Upper Gravity-Wave Absorbing Layer for NWP  
938 Applications, *Monthly Weather Review*, 176, 3987-4004, 2008.  
939

940 Klemp, J. B. and D. K. Lilly: Numerical simulation of hydrostatic mountain waves, *J.*  
941 *Atmos. Sci.*, 35, 78–107, 1978.  
942

943 Lin, Y., Farley, R., and Orville, H.: Bulk parameterization of the snow field in a cloud  
944 model, *J. Appl. Meteor. Clim.*, 22, 1065–1092, 1983.  
945

946 Marshall, J. S., and W. McK. Palmer, 1948: The distribution of raindrops with size. *J.*  
947 *Meteor.*, 5, 165–166.  
948

949 Matte, Dominic; Laprise, René; Thériault, Julie M.; Lucas-Picher, Philippe (2017). *Spatial*  
950 *spin-up of fine scales in a regional climate model simulation driven by low-resolution*  
951 *boundary conditions. Climate Dynamics*, 49(1-2), 563–574. doi:10.1007/s00382-016-  
952 3358-2

953

954 Mlawer, E. J., S. J. Taubman, P. D. Brown, M. J. Iacono, and S. A. Clough, 1997:  
955 Radiative transfer for inhomogeneous atmospheres: RRTM, a validated correlated-k  
956 model for the longwave. *J. Geophys. Res.*, 102, 16,663-16,682

957  
958 Nogherotto, R., Tompkins, A.M., Giuliani, G., Coppola, E. and Giorgi, F.: Numerical  
959 framework and performance of the new multiple-phase cloud microphysics scheme in  
960 RegCM4. 5: precipitation, cloud microphysics, and cloud radiative effects. *Geoscientific*  
961 *Model Development*, 9(7), 2533-2547, 2016  
962  
963 Oleson, K. W., Lawrence, D. M., Bonan, G. B., Drewniak, B., Huang, M., Koven, C. D.,  
964 Levis, S., Li, F., Riley, W. J., Subin, Z. M., Swenson, S. C., Thornton, P. E., Bozbiyik, A.,  
965 Fisher, R., Kluzek, E., Lamarque, J. -F., Lawrence, P. J., Leung, L. R., Lipscomb, W.,  
966 Muszala, S., Ricciuto, D. M., Sacks, W., Sun, Y., Tang, J., and Yang, Z. -L: Technical  
967 Description of version 4.5 of the Community Land Model (CLM), Ncar Technical Note  
968 NCAR/TN-503+STR, National Center for Atmospheric Research, Boulder, CO, 422 pp,  
969 DOI: 10.5065/D6RR1W7M, 2013.  
970  
971 Pal JS, Small E, Eltahir E (2000) Simulation of regional-scale water and energy budgets:  
972 representation of subgrid cloud and precipitation processes within RegCM. *J Geo-phys*  
973 *Res* 105: 29579–29594  
974  
975 Pal JS et al (2007) The ICTP RegCM3 and RegCNET: regional climate modeling for the  
976 developing world. *Bull Am Meteorol Soc* 88:1395–1409  
977  
978 Pichelli, E., Coppola, E., Sobolowski, S. *et al.* The first multi-model ensemble of regional  
979 climate simulations at kilometer-scale resolution part 2: historical and future simulations  
980 of precipitation. *Clim Dyn* (2021). <https://doi.org/10.1007/s00382-021-05657-4>  
981  
982 Prein, Andreas F. and Andreas Gobiet (2017). 'Impacts of uncertainties in European  
983 gridded precipitation observations on regional climate analysis'. In: *International Journal*  
984 *of Climatology*. ISSN: 10970088. DOI: 10.1002/joc.4706  
985  
986 Prein, A. F. et al. A review on regional convection-permitting climate modeling:  
987 demonstrations, prospects, and challenges. *Rev. Geophys.* 53, 323–361 (2015).

988

989 Ralph, F. M., P. J. Neiman, G. A. Wick, S. I. Gutman, M. D. Dettinger, D. R. Cayan, and A.  
990 B. White, 2006: Flooding on California's Russian River: Role of atmospheric rivers.  
991 *Geophys. Res. Lett.*, 33, L13801, <https://doi.org/10.1029/2006GL026689>

992

993 Ralph, F. M., M. D. Dettinger, M. M. Cairns, T. J. Galarneau, and J. Eylander, 2018:  
994 Defining "atmospheric river": How the Glossary of Meteorology helped resolve a debate.  
995 *Bull. Amer. Meteor. Soc.*, 99, 837–839, <https://doi.org/10.1175/BAMS-D-17-0157.1>

996

997 Rutledge, S. A., and P. V. Hobbs, 1983: The mesoscale and microscale structure and  
998 organization of clouds and precipitation in midlatitude cyclones. Part VIII: A model for the  
999 "seeder-feeder" process in warm-frontal rainbands. *J. Atmos. Sci.*, 40, 1185–1206.

1000

1001 Skamarock WC, Klemp JB, Dudhia J, Gill DO, Barker DM, Duda MG, Huang XY, Wang  
1002 W, Powers JG. 2008. 'A description of the advanced research WRF version 3', Technical  
1003 Note NCAR/TN-475+STR. NCAR: Boulder, CO

1004

1005 Schwartz, C. S., 2014: Reproducing the September 2013 record-breaking rainfall over  
1006 the Colorado Front Range with high-resolution WRF forecasts. *Wea. Forecasting*, 29,  
1007 393–402, <https://doi.org/10.1175/WAF-D-13-00136.1>

1008

1009 Sitz, L. E., F. Sante, R. Farneti, R. Fuentes-Franco, E. Coppola, L. Mariotti, M. Reale, et  
1010 al. 2017. "Description and Evaluation of the Earth System Regional Climate Model  
1011 (RegCM-ES)." *Journal of Advances in Modeling Earth Systems*.  
1012 doi:10.1002/2017MS000933

1013

1014 Song Y, Semazzi HMF, Xie L, Ogallo LJ, 2004: A coupled regional climate model for the  
1015 Lake Victoria Basin of East Africa. *Int. J. Climatol.* 24: 57-75.

1016

1017 Sun X, Xie L, Semazzi F, Liu B, 2015: Effect of Lake Surface Temperature on the Spatial  
1018 Distribution and Intensity of the Precipitation over the Lake Victoria Basin. Mon. Wea.  
1019 Rev. 143: 1179-1192.  
1020

1021 Sundqvist, H., Berge, E., and Kristjansson, J.: Condensation and cloud parameterization  
1022 studies with a mesoscale numerical weather prediction model, Mon. Weather Rev., 117,  
1023 1641–1657,1989.  
1024

1025 Talling, J. F. (1969) The incidence of vertical mixing, and some biological and chemical  
1026 consequences, in tropical African lakes, Verh. Int. Ver. Limnol. 17, 998-1012 DOI:  
1027 10.1080/03680770.1968.11895946  
1028

1029 Tiedtke, M., 1989, A comprehensive mass flux scheme for cumulus parametrization in  
1030 large-scale models. Mon. Weather Rev., 117, 1779–1800  
1031

1032 Tiedtke, M., 1993: Representation of Clouds in Large-Scale Models. Mon. Wea. Rev.,  
1033 121, 3040–3061, [https://doi.org/10.1175/1520-0493\(1993\)121](https://doi.org/10.1175/1520-0493(1993)121<3040:ROCILS>2.0.CO;2)  
1034

1035 Tiedtke, M., . 1996: An extension of cloud-radiation parameterization in the ECMWF  
1036 model: The representation of subgrid-scale variations of optical depth.Mon. Wea. Rev.,  
1037 124, 745–750  
1038

1039 Tompkins, A.: Ice supersaturation in the ECMWF integrated fore-cast system, Q. J. Roy.  
1040 Meteor. Soc., 133, 53–63, 2007  
1041

1042 Tripoli, G. J., and W. R. Cotton, 1980: A numerical investigation of several factors  
1043 contributing to the observed variable intensity of deep convection over south Florida. J.  
1044 Appl. Meteor., 19, 1037–1063.  
1045

1046 Williams PD. 2009. A proposed modification to the Robert–Asselin time filter. Mon.  
1047 Weather Rev. 137: 2538–2546

1048

1049 Weisman, M. L., C. Davis, W. Wang, K. W. Manning, and J. B. Klemp, 2008: Experiences  
1050 with 0–36-h explicit convective forecasts with the WRF-ARW model. *Wea. Forecasting*,  
1051 23, 407–437, <https://doi.org/10.1175/2007WAF2007005.1>

1052

1053 Weusthoff, T., F. Ament, M. Arpagaus, and M. W. Rotach, 2010: Assessing the benefits  
1054 of convection-permitting models by neighborhood verification: Examples from MAP D-  
1055 PHASE. *Mon. Wea. Rev.*, 138, 3418–3433, <https://doi.org/10.1175/2010MWR3380.1>.

1056

1057 Zeng X, Zhao M, Dickinson RE (1998) Intercomparison of bulk aerodynamic algorithms  
1058 for the computation of seasurface fluxes using TOGA COARE and TAO data. *J Clim* 11:  
1059 2628–2644

1060

1061 Zhu, Y., and R. E. Newell, 1998: A proposed algorithm for moisture fluxes from  
1062 atmospheric rivers. *Mon. Wea. Rev.*, 126, 725–735, [https://doi.org/10.1175/1520-0493\(1998\)126<0725:APAFMF>2.0.CO;2](https://doi.org/10.1175/1520-0493(1998)126<0725:APAFMF>2.0.CO;2).